

HAT-P-11b: A SUPER-NEPTUNE PLANET TRANSITING A BRIGHT K STAR IN THE *KEPLER* FIELD*

G. Á. BAKOS^{1,10}, G. TORRES¹, A. PÁL^{1,2}, J. HARTMAN¹, GÉZA KOVÁCS³, R. W. NOYES¹, D. W. LATHAM¹, D. D. SASSELOV¹,
B. SIPÓCZ^{1,2}, G. A. ESQUERDO¹, D. A. FISCHER⁴, J. A. JOHNSON^{5,11}, G. W. MARCY⁶, R. P. BUTLER⁷, H. ISAACSON⁴, A. HOWARD⁶,
S. VOGT⁸, GÁBOR KOVÁCS¹, J. FERNANDEZ¹, A. MOÓR³, R. P. STEFANIK¹, J. LÁZÁR⁹, I. PAPP⁹, AND P. SÁRI⁹

¹ Harvard-Smithsonian Center for Astrophysics, Cambridge, MA, USA; gbakos@cfa.harvard.edu

² Department of Astronomy, Eötvös Loránd University, Budapest, Hungary

³ Konkoly Observatory, Budapest, Hungary

⁴ Department of Physics and Astronomy, San Francisco State University, San Francisco, CA, USA

⁵ Institute for Astronomy, University of Hawaii, Honolulu, HI 96822, USA

⁶ Department of Astronomy, University of California, Berkeley, CA, USA

⁷ Department of Terrestrial Magnetism, Carnegie Institute of Washington, DC, USA

⁸ University of California Observatories/Lick Observatory, University of California at Santa Cruz, Santa Cruz, CA 95064, USA

⁹ Hungarian Astronomical Association, Budapest, Hungary

Received 2008 December 30; accepted 2010 January 11; published 2010 February 2

ABSTRACT

We report on the discovery of HAT-P-11b, the smallest radius transiting extrasolar planet (TEP) discovered from the ground, and the first hot Neptune discovered to date by transit searches. HAT-P-11b orbits the bright ($V = 9.587$) and metal rich ($[\text{Fe}/\text{H}] = +0.31 \pm 0.05$) K4 dwarf star GSC 03561–02092 with $P = 4.8878162 \pm 0.0000071$ days and produces a transit signal with depth of 4.2 mmag, the shallowest found by transit searches that is due to a confirmed planet. We present a global analysis of the available photometric and radial velocity (RV) data that result in stellar and planetary parameters, with simultaneous treatment of systematic variations. The planet, like its near-twin GJ 436b, is somewhat larger than Neptune ($17 M_{\oplus}$, $3.8 R_{\oplus}$) both in mass $M_p = 0.081 \pm 0.009 M_J$ ($25.8 \pm 2.9 M_{\oplus}$) and radius $R_p = 0.422 \pm 0.014 R_J$ ($4.73 \pm 0.16 R_{\oplus}$). HAT-P-11b orbits in an eccentric orbit with $e = 0.198 \pm 0.046$ and $\omega = 355^{\circ}2 \pm 17^{\circ}3$, causing a reflex motion of its parent star with amplitude $11.6 \pm 1.2 \text{ m s}^{-1}$, a challenging detection due to the high level of chromospheric activity of the parent star. Our ephemeris for the transit events is $T_c = 2454605.89132 \pm 0.00032$ (BJD), with duration 0.0957 ± 0.0012 days, and secondary eclipse epoch of 2454608.96 ± 0.15 days (BJD). The basic stellar parameters of the host star are $M_{\star} = 0.809^{+0.020}_{-0.027} M_{\odot}$, $R_{\star} = 0.752 \pm 0.021 R_{\odot}$, and $T_{\text{eff}\star} = 4780 \pm 50$ K. Importantly, HAT-P-11 will lie on one of the detectors of the forthcoming *Kepler* mission; this should make possible fruitful investigations of the detailed physical characteristic of both the planet and its parent star at unprecedented precision. We discuss an interesting constraint on the eccentricity of the system by the transit light curve and stellar parameters. This will be particularly useful for eccentric TEPs with low-amplitude RV variations in *Kepler*'s field. We also present a blend analysis, that for the first time treats the case of a blended transiting hot Jupiter mimicking a transiting hot Neptune, and proves that HAT-P-11b is not such a blend.

Key words: planetary systems – stars: individual (HAT-P-11, GSC 03561–02092) – techniques: photometric – techniques: spectroscopic

Online-only material: machine-readable tables

1. INTRODUCTION

Transiting extrasolar planets (TEPs) are uniquely valuable for understanding the nature of planetary bodies, because the transit light curve, combined with precise radial velocity (RV) measurements of the reflex motion of the parent star, yield unambiguous information on the true mass and radius of the planet, assuming that the stellar mass and radius are known. By inference, it is then possible to investigate the internal structure of these planets, as has been done by several teams trying to formulate and match theories to the observed bulk properties of known TEPs (e.g., Baraffe et al. 2008; Fortney et al. 2007; Burrows et al. 2007; Seager et al. 2007, and references therein). The transits across the face of the star enable a plethora

of scientific follow-up opportunities, such as detection of the atmospheres of these planets via transmission spectroscopy (Charbonneau et al. 2002), measurement of the stellar spin axis versus planetary orbit (Winn et al. 2005; Johnson et al. 2008) via the Rossiter–McLaughlin effect (Rossiter 1924; McLaughlin 1924), or measurement of their equilibrium temperature while they are occulted by their central stars (Charbonneau et al. 2005).

Photometric searches for TEPs have published some 50 such objects over the past eight years,¹² most of these with masses and radii in excess of that of Jupiter. Previously the smallest mass TEP discovered by the transit search method was HAT-P-1b with $M = 0.52 M_J$ and $R = 1.22 R_J$ (Bakos et al. 2007), recently superseded by the discovery of WASP-11/HAT-P-10b with $M = 0.46 M_J$ (West et al. 2009; Bakos et al. 2009). The smallest radius planet detected by ground-based transit searches was HAT-P-3b (Torres et al. 2007) with $R = 0.89 R_J$, and the smallest radius planet from the space is Corot-7b (Leger et al. 2009).

* Based in part on observations obtained at the W. M. Keck Observatory, which is operated by the University of California and the California Institute of Technology. Keck time has been granted by NAOA (A285Hr) and NASA (N128Hr).

¹⁰ NSF Fellow.

¹¹ NSF Postdoctoral Fellow.

¹² <http://www.exoplanet.eu/catalog-transit.php>

In the meantime, RV surveys have been reaching down to Neptune-mass planets, thanks to high precision and high signal-to-noise spectrographs that deliver radial velocities at the m s^{-1} level over an extended time, such as the High-Accuracy Radial velocity Planet Searcher (Mayor et al. 2003) on the ESO 3.6 m telescope, or High Resolution Echelle Spectrometer (HIRES) on Keck (Vogt et al. 1994). It was a major advance when Santos et al. (2004) discovered the $M_p \sin i = 14 M_\oplus$ planet around μ Ara, McArthur et al. (2004) detected a Neptune-mass planet around 55 Cnc, and Butler et al. (2004) found a $\sim 21 M_\oplus$ mass planet around GJ 436. These were followed by further exo-Neptune discoveries, such as the three Neptune planetary system around HD 69830 found by Lovis et al. (2006).

Recently, the detection threshold of RV searches has reached even below that of super-Earths ($M \lesssim 10 M_\oplus$). Rivera et al. (2005) found a $\sim 7.5 M_\oplus$ super-Earth orbiting the nearby M dwarf GJ 876. Udry et al. (2007) found a $5 M_\oplus$ and an $8 M_\oplus$ mass planet in a triple planetary system around GJ 581. Finally, Mayor et al. (2009) discovered a triple super-Earth system with 4.2, 6.9, and 9.2 earth masses around HD 40307. Altogether, as of writing, some 20 objects with minimum mass $M_p \sin i < 0.1 M_J = 31.8 M_\oplus$ have been detected by the RV technique.

RV detections are routinely checked for transit events by the discovery teams, or by the transitsearch.org collaboration of amateur/professional astronomers (Seagroves et al. 2003). A few successful detections have been reported.¹³ One such case is HD 189733b, a $1.13 M_J$ planet around a K dwarf, discovered by Bouchy et al. (2005) via the RV method, and confirmed to transit by the same team via the Rossiter–McLaughlin effect, and then via follow-up photometric observations. Another example is the 21.2 day period eccentric planet HD 17156b found by Fischer et al. (2007), with transits detected by Barbieri et al. (2007) through transitsearch.org. A third example, HD 149026b, is a transition object between Jupiter-mass and Neptune-mass planets, in the sense that it is a hot Saturn with $M_p = 0.36 M_J$ (or about 1.2 times the mass of Saturn) and $R_p = 0.71 R_J$. The RV detection by Sato et al. (2005) was followed by discovery of the 0.3% deep transits by the same team.

Among the ~ 20 Neptune-mass objects found by RV searches, only one is known to transit. This is GJ 436b, whose transits were recovered by Gillon et al. (2007a). GJ 436b is thus an extremely valuable and unique object, the only Neptune-mass planet other than our own Uranus and Neptune, where the radius has been determined ($R \approx 4.9 R_\oplus$ or $4.2 R_\oplus$; Bean et al. 2008; Torres et al. 2008, respectively, hereafter B08 and T08), and its internal structure investigated (e.g., Baraffe et al. 2008). Based on these results, GJ 436b is a super-Neptune with $\sim 22 M_\oplus$ total mass with extreme heavy element enrichment, and only $\sim 10\%$ mass contribution by a H/He envelope.

One of the wide-field surveys involved in the detection of TEP’s is the HATNet survey (Bakos et al. 2002, 2004), which currently operates six small fully automated wide-field telescopes. One station is the Fred Lawrence Whipple Observatory (FLWO) of the Smithsonian Astrophysical Observatory (SAO) on Mt. Hopkins in Arizona with four telescopes (HAT-5, HAT-6, HAT-7, HAT-10), and the other is the rooftop of the Submillimeter Array Hangar (SMA) of SAO atop Mauna Kea, Hawaii. These telescopes are modest 0.11 m diameter $f/1.8$ focal ratio telephoto lenses that are using front-illuminated CCDs at 5 minute integration times.

Here we report on HATNet’s discovery of HAT-P-11b, the second transiting hot Neptune known. HAT-P-11b orbits the bright ($V = 9.59$) K dwarf star GSC 03561–02092 (hereafter called HAT-P-11) with a period of 4.8878 days, and when it transits the star it causes a dip in the stellar light curve of about 4.2 mmag. HAT-P-11b is certainly the smallest radius planet found by ground-based transit searches, the only planet known with smaller radius being Corot-7b (Leger et al. 2009). Importantly, the coordinates of the parent star place it on one of the detectors of the forthcoming *Kepler* mission; this should allow a broad range of useful follow-on observations to characterize both the planetary system and the parent star. Because HAT-P-11 is a bright star, but still conveniently below the bright limit of the *Kepler* mission, the extraordinary precision of repeated measurements made over several years should lead to very accurate characterization of the system. We note that HAT-P-11b would have not been detected by HATNet if it orbited a significantly earlier star, such as the typical F and G dwarf stars making up the bulk of the HATNet transit candidates.

The layout of the paper is as follows. First we describe in Section 2 the observational data that led to the discovery of HAT-P-11b, including the photometric discovery data, the reconnaissance spectroscopic observations, the photometric follow-up, and the high-resolution and high signal-to-noise (S/N) spectroscopy. Then we determine the parameters of the host star HAT-P-11 (GSC 03561–02092) in Section 3 by exploring a number of alternate ways. In Section 4, we investigate whether the observational data are due to a system that mimics planetary transits, and prove that this is not the situation, and HAT-P-11b is a *bona-fide* planet. We go on in Section 5 to perform global modeling of the data to determine system parameters, such as the orbital and planetary parameters. We elaborate on treating the systematic variations in an optimal way, and present a full analysis that takes them into account (Sections 5.2, 5.1, and the Appendix). Finally, we discuss the implications of our findings in the discussion (Section 6).

2. OBSERVATIONS

2.1. Photometric Discovery

The $8^\circ 4' \times 8^\circ 4'$ region around GSC 03561–02092, a field internally labeled as “G155,” was observed on a nightly basis in two seasons, whenever weather conditions permitted. First, during the Fall of 2004, we acquired 1213 frames with the HAT-6 instrument located at FLWO, and 4091 frames with HAT-9 located at SMA, Mauna Kea. We revisited the field in 2005, and acquired an additional 6166 frames with HAT-9. Altogether we gathered 11470 5 minute exposures at a 5.5 minute cadence. This unusually rich data set was motivated by the overlap of G155 with the field of view (FOV) of the future *Kepler* mission.

The calibration of the HATNet frames was done utilizing standard procedures based on IRAF.¹⁴ The calibrated frames were then subjected to star detection and astrometry, as described by Pál & Bakos (2006). Aperture photometry using three apertures was performed on each image at the fixed positions of the stellar centroids, as derived from the Two Micron All Sky Survey (2MASS) catalog (Skrutskie et al. 2006) and the individual astrometric solutions relating the pixel coordinates to the world coordinate (ICRS) system of 2MASS. We extracted photometry for all 125,000 stars down to $I \lesssim 14$ that fell in the field. The

¹³ Of course, the first and most prominent one being HD 209458b (Charbonneau et al. 2000; Henry et al. 2000).

¹⁴ IRAF is distributed by the National Optical Astronomy Observatory, which is operated by the Association of Universities for Research in Astronomy, Inc., under cooperative agreement with the National Science Foundation.

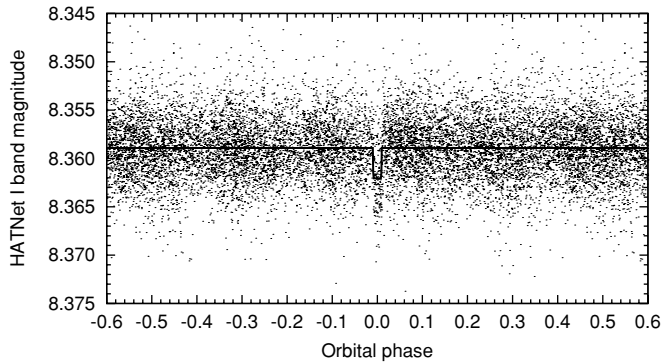


Figure 1. HATNet discovery light curve of HAT-P-11 exhibiting 11470 individual measurements at 5.5 minute cadence. The unbinned instrumental *I*-band photometry was obtained with the HAT-6 (Arizona) and HAT-9 (Hawaii) telescopes of HATNet (see the text for details), and folded with the period of $P = 4.8878162$ days, which is the result of the global fit described in Section 5. Zero orbital phase corresponds to the center of the transit. Superimposed is the so-called “PIP3” analytic model that was used to describe the HATNet data (an approximation of the Mandel & Agol (2002) analytic formulae; see Section 5.1).

raw instrumental magnitudes m_r of each individual frame were transformed to a reference frame by fourth-order polynomials in *X* and *Y*, and first order in color. The fitted magnitudes m_f yielded by the above smooth fit are used for generating the time versus m_f light curves.

These light curves have a noise characteristic that is sometimes referred to as pink noise (Pont et al. 2006), because it is a combination of Gaussian white noise (due to e.g., photon noise) and a correlated red noise (due to e.g., spatial drift of stars and uncorrected flatfield effects). The red noise is often referred to as trends or systematic variations. Trends in the light curves have an adverse effect on detecting shallow transiting signals: they mask the real signal, and when phase-folded with a trial period they can also mimic transit signals. Furthermore, for photometric follow-up data, the trends can lead to large systematic errors in the transit parameter determination, such as in the impact parameter or the depth of the transit. Thus, proper treatment of systematic variations is crucial for both discovery and accurate follow-up characterization, especially for the shallow (4.2 mmag) transit of a hot Neptune presented in this paper. The two basic methods we have employed are the external parameter decorrelation (EPD) technique, briefly described earlier in Bakos et al. (2007), and the trend filtering algorithm (TFA; Kovács et al. 2005). The technical details and some new definitions are given in the Appendix.

The HATNet light curves were decorrelated against trends using the EPD technique (in constant EPD mode), and subsequently by a simple global TFA (without reconstruction, and separately from the EPD). For the brightest stars in the field we achieved a photometric precision of 2.9 mmag at 5.5 minute cadence. The light curves were searched for periodic box-like signals using the box least-squares transit search method (BLS; see Kovács et al. 2002). The BLS frequency spectrum of GSC 03561–02092 (also known as 2MASS 19505021+4804508; $\alpha = 19^{\text{h}}50^{\text{m}}50^{\text{s}}.21$, $\delta = +48^{\circ}04^{\text{m}}50^{\text{s}}.8$; J2000) showed a number of significant peaks, the highest one at 0.03148 [c/d] (31.76 day period), and the second one at ~ 0.2046 [c/d] (4.8878 days). Fortunately, we inspected the second peak, and found the corresponding transit (Figure 1) with a depth of 4.2 mmag, worthy of follow-up. The dip had a relative duration (first to last contact) of $q \approx 0.0206$, equivalent to a total duration of $Pq \approx 2.41$ hr. The signal was confirmed with subsequent reconstructive TFA using

a trapeze-shaped model function, being the most significant periodicity in the data (the 31.76 day signal was probably due to a left-over systematic). The rms of the TFA processed light curve was ~ 3.2 mmag, making the detection of the 4.2 mmag transit dip rather challenging, but still robust with $S/N = 11.4$. To our best knowledge, this is the shallowest transit signal found by ground-based transit searches that belongs to a confirmed planet. HD 149026, with an even shallower transit signal (Winn et al. 2008) was first detected via spectroscopy (Sato et al. 2005). The second shallowest planetary transit found by the transit search method is HAT-P-2b (Bakos et al. 2007). We note that on occasion HATNet has found even shallower transiting signals (down to 2 mmag depth) where the transit was real, but was due to a blended system.

2.2. Follow-up Reconnaissance Spectroscopy

Following the procedures described in Latham et al. (2009), we used the CfA Digital Speedometers (DS; Latham 1992), mounted on the 1.5 m Wyeth Reflector at the Oak Ridge Observatory in Harvard, Massachusetts, and on the 1.5 m Tillinghast Reflector at FLWO, to obtain low S/N ratio high-resolution spectra. Altogether five spectra were obtained between 2001 December 17 and 2007 June 5 (the first observations were obtained for a different project to survey dwarfs in the solar neighborhood that might be suitable targets for SETI). The signal-to-noise ratios ranged from 10 to 18 per spectral resolution element of 8.5 km s^{-1} .

Reconnaissance spectroscopy is an important step in weeding out astrophysical false positive systems that mimic planetary transits. Stellar parameter determination can distinguish between dwarf and giant stars via the measurement of surface gravity $\log g_*$, and thus eliminate systems where the light curve of an eclipsing binary is blended with a giant star, or where the transit signal seen in our data may not be real, as it is physically not feasible to orbit around (and outside) the giant star with such a short period. In addition, large RV variations (of the order of several km s^{-1}) are indicative of orbital motion due to stellar companions rather than planets orbiting a star. Fine analysis of the spectra can also reveal stellar triple systems. Finally, the rapid rotation of a host star, as may be indicated by the rotational broadening of the spectra, is often correlated with a stellar companion that is massive enough to synchronize the rotation with the orbital motion.

HAT-P-11 survived all these steps, and the RV measurements showed an rms residual of 0.29 km s^{-1} , consistent with no detectable RV variation. Initial atmospheric parameters for the star, including the effective temperature $T_{\text{eff}\star} = 4750 \pm 125 \text{ K}$, surface gravity $\log g_* = 4.5 \pm 0.25$ (cgs), and projected rotational velocity $v \sin i = 0.0 \text{ km s}^{-1}$, were derived as described by Latham et al. (2009). The mean line-of-sight velocity of the star was $\Gamma = -63.56 \pm 0.29 \text{ km s}^{-1}$ on an absolute scale.

2.3. Photometric Follow-up Observations

Photometric follow-up observations are important (1) to perform independent confirmation of the initial detection, (2) to allow for accurate characterization of the system (see also Section 5), (3) to help eliminate blend scenarios (Section 4), and, if multiple events are observed, (4) to possibly average out extra variations of the light curve due to spots. Since the transit of HAT-P-11 was originally detected with the 11 cm diameter HATNet telescopes (although when phase-folding many events), it is certainly feasible to confirm a single transit

Table 1
Photometric Follow-up Observations of HAT-P-11

Local Date	Instrument	Filter	N_{tr}	Type
2007.0902	FLWO12	z	0	OIBEO
2007.0907	FLWO12	z	1	--BEO
2007.1021	FLWO12	z	10	OIBE(O)
2008.0518	FLWO12	z	53	(OI)BEO
2008.0603*	Schmidt	I_C	56	(OIB--)
2008.0701	FLWO12	z	62	OIB--
2008.0829*	Schmidt	I_C	74	(OIBEO)
2008.0903	Schmidt	I_C	75	OIBEO
2008.1002	FLWO12	z	81	OIBEO
2008.1007	FLWO12	z	82	OIBEO
2008.1115	FLWO12	z	90	OIB--
2008.1120	FLWO12	r	91	OIBEO

Notes. Dates marked with “*” were of poor quality, and not used in the analysis. N_{tr} gives the transit event number, counted from the zeroth follow-up event on 2007 September 2. The Type column shows which parts of the transit were caught: Out-of-transit (OOT), Ingress, Bottom, Egress, OOT. Parentheses mark marginal data quality.

with a 1 m class telescope. However, acquiring a high-quality observation of the 4.2 mmag transit dip in the light of a star as bright as $V = 9.59$ is quite challenging. An accurate and highly precise light curve is essential for eliminating blend scenarios, and then for determining the physical parameters of the transiting planet–star system. In general, the shallower the transit, the wider the range of possible blends (i.e., more than two body systems) that can mimic the observed transit. Some of these can only be distinguished by subtle effects, such as the duration of ingress/egress, and accurate depth and shape of the transit.

For these reasons, we launched an extensive photometry follow-up campaign, and attempted transit observations of HAT-P-11b altogether 12 times in 2007 and 2008, leading to ~ 10 successful observations of partial or full transits (see Table 1). We primarily used the FLWO 1.2 m telescope and the KeplerCam CCD in Sloan z band, with exposure times of ~ 10 s and read-out time of 12 s. The last observation on 2008 November 20/21 MST was taken through Sloan r band to complement our blend analysis (Section 4). We also observed transits 3 times using the 0.6 m Schmidt telescope of Konkoly Observatory at the Piszkestető Mountain Station. These observations were taken through I_C band, and the only useful data set proved to be the one from 2008 September 3/4 CET.

Data were reduced in a similar manner as for the HATNet data (Section 2.1), and as described in Bakos et al. (2009). Following bias and flat calibration, we derived an initial first-order astrometrical transformation between the ~ 750 brightest stars and the 2MASS catalog. The position of HAT-P-11 in the 2MASS catalog was corrected for each observed epoch before deriving the astrometry due to its moderately high proper motion (263.32 ± 1.31 mas yr $^{-1}$; Perryman et al. 1997). Photometry was carried out for all stars in the field using three apertures that were adjusted each night to match the observing conditions (sky background, profile width). For the nights with good seeing, one aperture was kept small to avoid the faint neighbor 2MASS 19505049+4805017 currently at approx 6" distance (see Section 4). Instrumental magnitudes were transformed to a photometric reference frame (selected to be at low air mass, low sky background, etc.) using a first-order polynomial in the X, Y

pixel coordinates and the 2MASS $J - K$ color of ~ 600 stars. The transformation was iteratively determined by weighting with individual Poisson noise errors of the stars, and rejecting 3σ outliers, plus eliminating the main target and its faint neighbor from the fit. The smooth fit was repeated based on the ~ 180 best stars, using the median of the individual light-curve magnitude values as a new reference system, and weighting the fit with the rms of the light curves (i.e., substituting the former Poisson errors).

The FLWO 1.2 m KeplerCam observations usually result in high-quality photometry of $\sim 1\%$ deep planetary transits (see e.g., Latham et al. 2009; Bakos et al. 2009), because of the large FOV ($= 23' \times 23'$) with many potential comparison stars, fine pixel resolution ($0''.336$ pixel $^{-1}$), good quality and high quantum efficiency CCD (monolithic, $4k \times 4k$ Fairchild 486 chip), good sky conditions from FLWO, the fast readout through four channels, and careful data processing. The performance on this very shallow transit of a fairly bright star, however, turned out to be slightly sub-optimal with some residual trends, necessitating diverse application of the EPD and TFA methods. Since these were part of our global modeling of the data, including the HATNet and RV data, they are detailed later in Section 5 and in the Appendix. The follow-up light curves after applying simultaneous EPD–TFA with per night coefficients for EPD and global coefficients for TFA are displayed in Figure 2; the photometric data is provided in Table 2. The model function (denoted as $m_0(\vec{p}, t_i)$ in Equation (A1) in the Appendix) in the simultaneous EPD–TFA fit is an analytical transit model from Mandel & Agol (2002).

2.4. High-Resolution, High S/N Spectroscopy

We started observations of HAT-P-11 on 2007 August 22 with the HIRES instrument (Vogt et al. 1994) on the Keck-I telescope located on Mauna Kea, Hawaii. It was soon realized that the target is unusually complicated because of the small RV amplitude with respect to the moderate velocity jitter due to the active K dwarf star, and also because of long-term trend(s) present. Thus, HAT-P-11 has been extensively observed over the past two years, and we have gathered altogether 50 spectra and three template observations (see Table 3). This is 5–10 times the number of spectra collected for a typical HATNet transit candidate.

The width of the spectrometer slit used on HIRES was $0''.86$, resulting in a resolving power of $\lambda/\Delta\lambda \approx 55,000$, with a wavelength coverage of ~ 3800 – 8000 Å. The iodine gas absorption cell was used to superimpose a dense forest of I_2 lines on the stellar spectrum and establish an accurate wavelength fiducial (see Marcy & Butler 1992). Relative RVs in the solar system barycentric frame were derived as described by Butler et al. (1996), incorporating full modeling of the spatial and temporal variations of the instrumental profile. The final RV data and their errors as a function of barycentric Julian date are listed in Table 3. It is reassuring that a simple Fourier analysis of the RV data *without* prior assumption on any periodic event yields a primary period of 4.888 ± 0.019 days, confirming the same periodic phenomenon that is present in the independent data set consisting of the discovery and follow-up photometry.¹⁵

Based on the numerous observations of a transit-like event in the photometry, our initial physical model was thus a single body orbiting and transiting the star, causing both the RV

¹⁵ The uncertainty of the period was simply derived from the full width at half-magnitude of the appropriate peak in the spectrum.

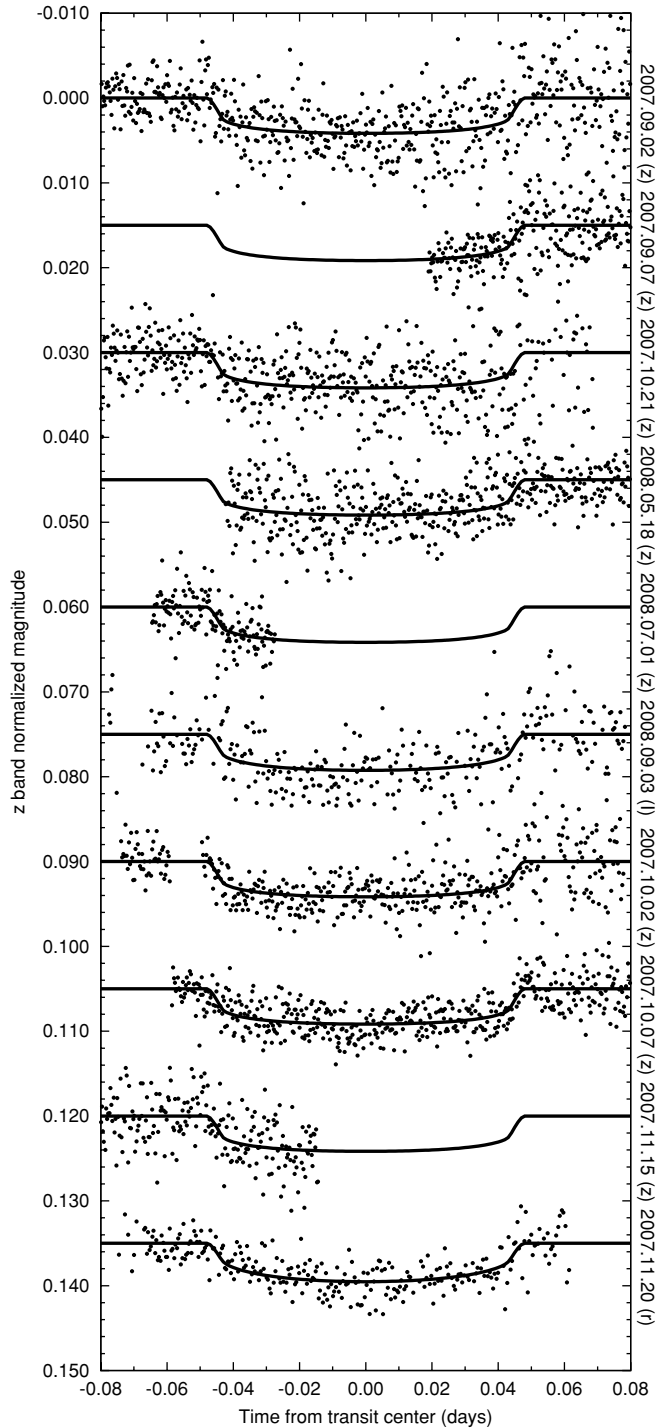


Figure 2. Unbinned instrumental transit photometry follow-up light curves acquired by the KeplerCam at the FLWO 1.2 m telescope (in Sloan z band, and Sloan r band) and by the 0.6 m Schmidt telescope at Piszkestető, Hungary (in I_C band). Superimposed is the best-fit transit light-curve model, yielded by the global analysis described in Section 5. The light curves have been subject to global EPD and TFA corrections using an analytical transit model for the intrinsic signal (see the Appendix).

variations and the transits. The RV variations induced on the parent star can be characterized by six parameters: the period P , the center of transit T_c (i.e., the phase of the RV curve), the semi-amplitude K , the RV zero-point γ , and the Lagrangian orbital elements $(k, h) = e \times (\cos \omega, \sin \omega)$. An orbital fit to the RV data without any constraints from the photometry yielded the following values: $P = 4.8896 \pm 0.0017$ days,

Table 2
Follow-up Photometry for HAT-P-11

BJD	Mag	Error	Raw Mag	Filter	N_{tr}	Instrument
2454346.61746	-0.00134	0.00064	-0.00082	z	0	FLWO12
2454346.61771	-0.00228	0.00064	-0.00234	z	0	FLWO12
2454351.74387	0.00545	0.00066	0.00615	z	1	FLWO12
2454351.74414	0.00320	0.00066	0.00134	z	1	FLWO12
2454395.58419	-0.00509	0.00068	-0.00078	z	10	FLWO12
2454395.58575	-0.00042	0.00062	-0.00170	z	10	FLWO12
2454605.84905	0.00287	0.00065	0.00393	z	53	FLWO12
2454605.84933	0.00280	0.00065	0.00763	z	53	FLWO12
2454649.81716	0.00186	0.00069	0.00104	z	62	FLWO12
2454649.81742	0.00168	0.00069	-0.00059	z	62	FLWO12
2454713.34579	-0.00234	0.00096	0.00018	I	75	Schmidt
2454713.34612	-0.00136	0.00099	0.00131	I	75	Schmidt
2454742.67630	-0.00239	0.00053	-0.00358	z	81	FLWO12
2454742.67664	-0.00049	0.00053	-0.00093	z	81	FLWO12
2454747.57949	0.00194	0.00054	-0.00019	z	82	FLWO12
2454747.57981	-0.00251	0.00054	-0.00376	z	82	FLWO12
2454786.57057	0.00386	0.00061	0.00543	z	90	FLWO12
2454786.57106	0.00042	0.00061	0.00307	z	90	FLWO12
2454791.55380	0.00134	0.00050	0.00048	r	91	FLWO12
2454791.55562	-0.00340	0.00050	-0.00356	r	91	FLWO12

Notes. Column 1: barycentric Julian Day; Column 2: best-detrended magnitude, normalized to 0.0 OOT; Column 3: estimated error in the best magnitude; Column 4: magnitude before detrending (denoted as m_f in the text); Column 6: transit number. See Table 1.

(This table is available in its entirety in a machine-readable form in the online journal. A portion is shown here for guidance regarding its form and content.)

Table 3
Relative Radial Velocity Measurements of HAT-P-11

BJD	RV (m s^{-1})	σ_{RV} (m s^{-1})	O-C (m s^{-1})	BS (m s^{-1})	σ_{BS} (m s^{-1})	S
2454335.89332	8.31	1.10	1.82	-2.40	5.32	0.603
2454335.89997	8.61	1.17	2.03	-2.70	5.38	0.604
2454336.74875	-3.12	1.12	-6.29	-17.80	6.29	0.614
2454336.25715	-1.30	5.27	0.616
2454336.86162	-0.34	1.11	-1.36	-1.74	5.41	0.613
...
2454790.68835	22.38	1.31	0.04	-8.66	5.76	0.621

(This table is available in its entirety in a machine-readable form in the online journal. A portion is shown here for guidance regarding its form and content.)

$T_c = 2454552.04 \pm 0.16$ (BJD), $K = 13.1 \pm 2.1 \text{ m s}^{-1}$, $\gamma = 0.9 \pm 0.8 \text{ m s}^{-1}$ (arbitrary scale), $k = 0.28 \pm 0.12$, and $h = 0.09 \pm 0.09$.

Later (Section 5) we present a global modeling of the data, where joint analysis of the photometry and RV data is performed. This yields precise P and T_c parameters that are almost entirely constrained by the photometric data (notably the sharp ingress/egress features), with virtually no coupling from the RV data. The knowledge of period and phase from photometry is a very tight constraint in the analysis of the RV data, yielding significant improvement on determination of the other orbital parameters. It is thus well justified to analyze the RV data separately by fixing the ephemeris to that determined by the photometry, and assuming that there is an eccentric orbital motion present. In addition, we can also investigate whether our initial model correctly described the physics of the system, and whether there are other signals present in the RV data.

Along these lines, our refined model for the RV data was an eccentric orbital motion with P and T_c fixed to those values

found from the global modeling (and primarily constrained by the photometry), plus a sinusoidal motion of the form $A_2 \sin(f_2 t) + B_2 \cos(f_2 t)$ (equivalent to $A'_2 \sin(f_2 t + \phi)$, but linear in the fitted A_2 and B_2 parameters). We searched the f_2 domain by fitting γ , K , k , h (eccentric orbit parameters) and A_2 , B_2 at each f_2 , and noting the χ^2 . This “frequency scan” located a number of significant peaks with small inverse χ^2 (Figure 3, upper panel), the most significant being $f_2 = 0.9602 \pm 0.0009$. We suspected that the peaks around 1 [c/d] might be due to a long-term trend in the RV, sampled with a daily and lunar-cycle periodicity. To test this effect, we generated a mock signal by co-adding an analytic eccentric orbital motion, a long-term RV drift, and Gaussian noise, and sampled these at the exact times of the 50 Keck observations. We ran the same fitting procedure (Keplerian plus sinusoidal motion) in the above-described frequency scan mode on the mock data. Indeed, the drift appeared as a number of significant frequencies around 1 [c/d] (Figure 3(b)), their exact location depending on the amplitude of the drift and the random seed used to generate the noise. Then, we repeated the above analysis including a long-term drift in the fitted model function while performing the frequency scanning procedure (i.e., fitting at each frequency value that is being stepped on a grid).

The results are plotted in panel(c) of Figure 3, on the same scale as used in panels (a) and (b). It can be clearly seen that the magnitude of the residuals is definitely smaller and the strong structures disappeared. Using the mock data set, the results are almost the same (Figure 3(d)), confirming our assumptions that a long-term drift in the data causes aliases around 1 [c/d]. This is in line with the experience based on long-term monitoring of stars with Keck/HIRES: in nearly every case where there is either a planet or a long-term trend, a spurious spike appears in the periodogram at close to one day.

Note, however, that in spite of the clearing of peaks around 1 [c/d], the 0.9602 [c/d] peak remained present even after the simultaneous fit of a Keplerian orbit and a drift to the Keck data.

It is also interesting that the χ^2 of the fit with Keplerian plus f_2 sinusoid component is somewhat smaller than the fit with Keplerian plus long-term trend. The $f_2 = 0.9602$ [c/d] periodicity may be a real physical effect, or can be an alias of a real physical effect with a different period (rotation period, activity of star), or an alias of a systematic effect (lunar cycle, instrumental effect). Altogether we have three components to consider in the final model of the RV variations: (1) Keplerian orbit, (2) long-term drift, (3) $f_2 = 0.9602$ [c/d] periodicity.

The model of a Keplerian orbit and a long-term drift ((1)+(2)) has simple underlying physics by assuming an inner and an outer planets. The results of the orbital fit for this basic model are exhibited in Figure 4. The data folded with the $P = 4.8878162$ day period after removal of the best-fit drift is plotted in the top panel. Superimposed is the Keplerian orbit that is clearly eccentric. The orbital elements for this fit were: $K = 11.6 \pm 1.2 \text{ m s}^{-1}$, $k = e \cos \omega = 0.201 \pm 0.049$, $h = e \sin \omega = 0.051 \pm 0.092$, $\gamma = -0.4 \pm 0.8 \text{ m s}^{-1}$, and the best-fit value for the linear drift is $G_1 = 0.0297 \pm 0.0050 \text{ m s}^{-1} \text{ day}^{-1}$. Note that the K amplitude of the orbit is only $11.6 \pm 1.2 \text{ m s}^{-1}$. In order to have a reduced χ^2 value of 1.0, a jitter of 5.01 m s^{-1} has to be added to the formal errors.

We also derived an orbital fit with a full model of all three components (Keplerian, drift, short-period sinusoidal) so as to check the effect of f_2 on the orbital parameters. We found that the change in the orbital elements is insignificant, with a small decrease in their respective error bars: $K = 10.91 \pm 0.96 \text{ m s}^{-1}$, $k = e \cos \omega = 0.225 \pm 0.038$, $h = e \sin \omega = 0.069 \pm 0.072$,

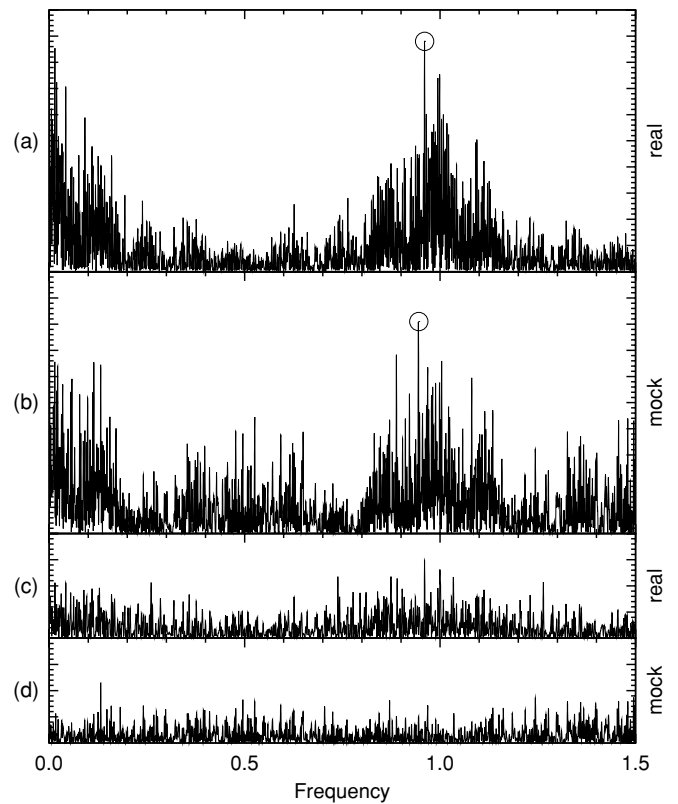


Figure 3. Top panel: inverse χ^2 as a function of f_2 frequency when fitting a combined Keplerian orbit with fixed P and T_c ephemeris, plus a sinusoidal component with f_2 frequency to the RV observations. The high peaks indicate good fit with small χ^2 . The 0.96 [c/d] peak is marked with a circle. Second panel: the same plot, but on a mock data set that consists of a Keplerian, a drift, and Gaussian noise. Third panel: same as the top panel, but the fitted model was extended by a drift with fitted slope. Much of the 1 [c/d] frequencies disappeared, but the one at e.g., 0.9602 [c/d] remained. Bottom panel: same as the second panel (mock data), with fitted model extended with a linear slope.

drift $G_1 = 0.0176 \pm 0.0056 \text{ m s}^{-1} \text{ day}^{-1}$, and the amplitude of the f_2 sinusoid is $5.7 \pm 1.3 \text{ m s}^{-1}$. The jitter value changed to 3.89 m s^{-1} .

We also investigated models with nonlinear drift, as characterized by G_2 quadratic and G_3 cubic terms, and found that these are insignificant based on the present data. We also checked for correlations between the RV residuals from the best fit, and the spectral bisector spans (BSs), and the S activity index, but found that these correlations were insignificant.

Given the fact that the origin of the f_2 periodicity (component 3) is unknown, and it is suspected to be an alias that may diminish by taking more data, plus the key orbital elements do not change significantly by taking it into account; in the rest of this paper, we adopted the simpler model of a Keplerian orbit (with $K = 11.6 \pm 1.2 \text{ m s}^{-1}$) and a long-term drift *without* the short-term periodicity.

3. PROPERTIES OF THE PARENT STAR

Knowledge of the parameters of the host star is important because it puts the relative quantities arising from the global modeling of the photometric and RV data (Section 5) on an absolute scale, since the planetary radius R_p is $\propto R_*$, and the planetary mass M_p is $\propto M_*^{2/3}$. Also, modeling of the photometric transit requires limb-darkening parameters. These may be fitted along with other parameters if the data are of high quality and allow it (Brown et al. 2001). Alternatively, limb-darkening

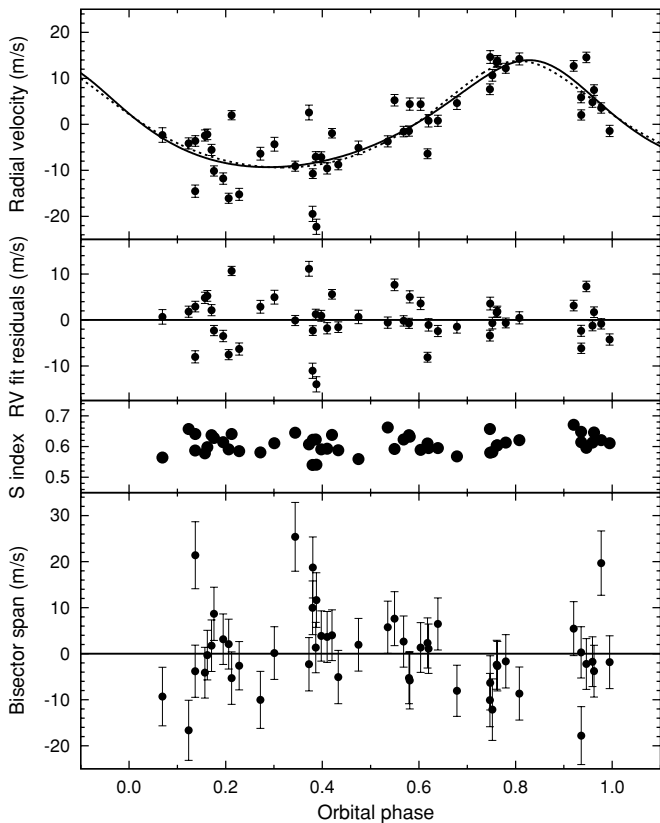


Figure 4. Top panel: RV measurements from Keck for HAT-P-11 after correction for a linear drift seen in the data. The measurements are folded using our best-fit ephemeris from global modeling of the photometry and RV data (see Section 5), and superimposed by our (eccentric) orbital fit. The center-of-mass velocity has been subtracted. The orbital phase is shifted to zero at the center of the transit. The error bars have not been inflated with the jitter (5.01 m s^{-1}). The dashed line (barely discernible from the thick line) is the orbital fit with the same ephemeris and K semi-amplitude, but using the refined k_C and h_C Lagrangian orbital elements (Section 5.5). Second panel: RV residuals after the orbital fit. Third panel: the S activity index of HAT-P-11 phase-folded. Bottom panel: BS for the Keck spectra plus the three template spectra, computed as described in the text. The mean value has been subtracted. The vertical scales on the lower and upper panels are the same.

coefficients are taken from look-up tables, such as that of Claret (2004), which depend on stellar atmospheric parameters, primarily effective temperature. Conversely, the presence of the planetary transit imposes constraints on the stellar parameters through the normalized semimajor axis a/R_* (and stellar density ρ_*) as yielded by the global modeling of the photometry, and, for eccentric orbits, the RV data (T08).

3.1. Basic Stellar Parameters

We employed the Spectroscopy Made Easy (SME) package of Valenti & Piskunov (1996) along with the atomic-line database of Valenti & Fischer (2005) to derive an initial value for the stellar atmospheric parameters. In this analysis, we used the iodine-free template spectrum obtained by the HIRES instrument on Keck I. The SME analysis of stellar spectra resulted in a stellar surface gravity $\log g_* = 4.7 \pm 0.1$ (CGS), metallicity $[\text{Fe}/\text{H}] = 0.32 \pm 0.06$ dex, effective temperature $T_{\text{eff}*} = 4850 \pm 50$ K, and the projected rotational velocity $v \sin i = 0.5 \pm 0.5 \text{ km s}^{-1}$. However, the $v \sin i$ value depends inversely on the assumed value of macro-turbulence v_{mac} in the star. The value of v_{mac} assumed in the SME derivation was 2.57 km s^{-1} , but for stars of type K0 or later, v_{mac} may be as small

as 1.3 km s^{-1} (e.g., Gray 1988). With that value of v_{mac} , $v \sin i$ could be as high as 2.7 km s^{-1} . Because of the indeterminacy of v_{mac} for HAT-P-11, we can conclude solely that HAT-P-11 is a relatively slow rotator and assign it a projected rotational velocity $v \sin i = 1.5 \pm 1.5 \text{ km s}^{-1}$, which encompasses both extremes of $v \sin i$ noted here.

At this stage, we could use the effective temperature as a color indicator and the surface gravity as a luminosity indicator, and determine the stellar parameters based on these two constraints using a set of isochrones. However, it has been shown (Sozzetti et al. 2007) that $\log g_*$ has a subtle effect on the spectral line shapes, and is usually not the best luminosity indicator. For planetary transits, the a/R_* normalized semimajor axis and related ρ_* mean stellar density typically impose a stronger constraint on possible stellar models (Sozzetti et al. 2007). (The use of a/R_* is discussed later in Section 3.2.) However, for HAT-P-11 there is an even better luminosity indicator, since it is a bright and nearby star with known parallax of small relative error. HAT-P-11 enters the *Hipparcos* catalog as HIP 97657 with reported parallax of $27.50 \pm 0.96 \text{ mas}$ (Perryman et al. 1997), equivalent to a distance of $36.4 \pm 1.3 \text{ pc}$ and distance modulus of $\Delta = 2.80 \pm 0.08$. Combination of the distance information with the apparent brightnesses in various photometric bands yields the absolute magnitude of the star, which is a tighter constraint on the luminosity than the $\log g_*$ or a/R_* constraints.

As regards apparent magnitude, the TASS (Droege et al. 2006) photometry for this star is $V_{\text{TASS}} = 9.587 \pm 0.071$ and $I_{\text{TASS}} = 8.357 \pm 0.050$, yielding $(V - I)_{\text{TASS}} = 1.230 \pm 0.087$. On the other hand, the Yonsei–Yale (YY) stellar evolution models (Yi et al. 2001; Demarque et al. 2004) indicate $(V - I)_{\text{YY,expect}} = 0.98 \pm 0.03$ for a star with $T_{\text{eff}*} \sim 4850$ K (based on the SME results). The 3σ inconsistency cannot be explained by interstellar reddening, since this is a close-by star. Thus, we opted not to use the TASS photometry in this analysis.

The 2MASS catalog (Skrutskie et al. 2006) provided much better agreement. The magnitudes reported in the 2MASS catalog have to be converted to the standard ESO system, in which the stellar evolution models (specifically the YY models) specify the colors. The reported magnitudes for this star are $J_{2\text{MASS}} = 7.608 \pm 0.029$, $H_{2\text{MASS}} = 7.131 \pm 0.021$, and $K_{2\text{MASS}} = 7.009 \pm 0.020$, which is equivalent to $J = 7.686 \pm 0.033$, $H = 7.143 \pm 0.028$, and $K = 7.051 \pm 0.021$ in the ESO photometric system (see Carpenter 2001). Thus, the converted 2MASS magnitudes yield a color of $(J - K) = 0.635 \pm 0.043$ that is within 1σ of the expected $(J - K)_{\text{YY,expect}} = 0.59 \pm 0.02$. We thus relied on the 2MASS K apparent magnitude and the parallax to derive an absolute magnitude of $M_K = 4.18 \pm 0.07$. The choice of K band was motivated by the longest wavelength with smallest expected discrepancies due to molecular lines in the spectrum of this K4 dwarf.

In practice, the isochrone search for the best-fit stellar parameters was done in a Monte Carlo way, by assuming Gaussian uncertainties for the *Hipparcos* parallax, $T_{\text{eff}*}$, $[\text{Fe}/\text{H}]$, the apparent 2MASS magnitudes, and the conversion coefficients by Carpenter (2001) that transform the 2MASS magnitudes to the standard K band. Lacking information, possible correlations between some of these parameters (e.g., $T_{\text{eff}*}$ and $[\text{Fe}/\text{H}]$) were ignored. A large set (~ 5000) of random Δ (distance modulus), $T_{\text{eff}*}$, $[\text{Fe}/\text{H}]$, and K values were generated, and for each combination we searched the stellar evolutionary tracks of the YY models for the best-fit stellar model parameters (such as M_* , R_* , etc.). For an unevolved K star there was no ambiguity in the solution, i.e., we did not enter a regime where isochrones

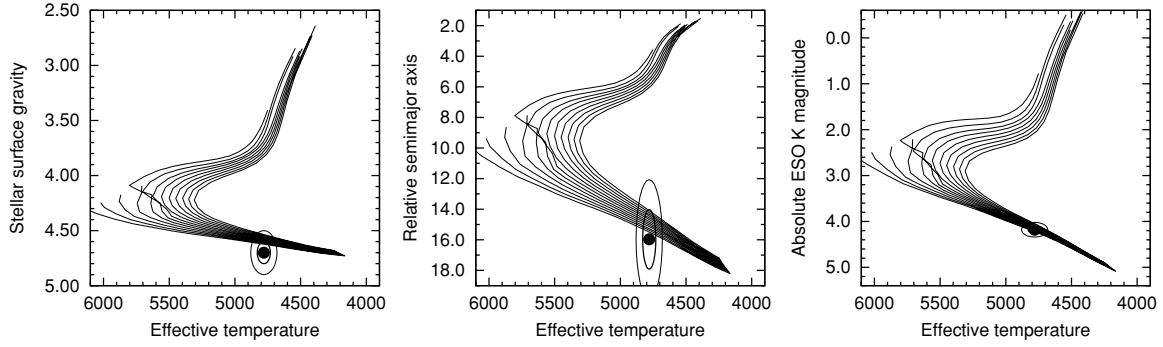


Figure 5. Three panels display the same YY isochrones between 2.0 and 14.0 Gyr for metal-rich, $[\text{Fe}/\text{H}] = +0.31$ stars, including masses between $0.65 M_{\odot} \leq M \leq 1.25 M_{\odot}$. The horizontal axis is effective temperature for all cases. The three panels show different choices of luminosity indicators (on the vertical axes). The observed values for the stellar parameters of HAT-P-11 are marked by the large filled circles, and the 1σ and 2σ confidence ellipsoids are also indicated. Left panel: the luminosity indicator (vertical axis) is the stellar surface gravity. Middle panel: the luminosity indicator is the geometric semimajor axis a/R_{\star} , as derived from the light-curve modeling (see Sections 3.2 and 5). Right panel: here the luminosity indicator is the M_K absolute K magnitude, based on the 2MASS catalog, transformations by Carpenter (2001), and the *Hipparcos* parallax. The tightest constraint on the isochrones is provided by the effective temperature (based on the SME analysis), and the absolute K magnitude photometry (right panel).

Table 4
Stellar Parameters for HAT-P-11

Parameter	Value	Source
$T_{\text{eff}\star}$ (K)	4780 ± 50	SME ^a
$[\text{Fe}/\text{H}]$	$+0.31 \pm 0.05$	SME
$v \sin i$ (km s^{-1})	1.5 ± 1.5	SME
M_{\star} (M_{\odot})	$0.81^{+0.02}_{-0.03}$	$Y^2+\text{Hip}+\text{SME}^b$
R_{\star} (R_{\odot})	0.75 ± 0.02	$Y^2+\text{Hip}+\text{SME}$
$\log g_{\star}$ (cgs)	4.59 ± 0.03	$Y^2+\text{Hip}+\text{SME}$
L_{\star} (L_{\odot})	0.26 ± 0.02	$Y^2+\text{Hip}+\text{SME}$
M_V (mag)	6.57 ± 0.09	$Y^2+\text{Hip}+\text{SME}$
Age (Gyr)	$6.5^{+5.9}_{-4.1}$	$Y^2+\text{Hip}+\text{SME}$
Distance (pc)	38.0 ± 1.3	$Y^2+\text{Hip}+\text{SME}^c$

Notes.

^a SME = ‘‘Spectroscopy Made Easy’’ package for analysis of high-resolution spectra (Valenti & Piskunov 1996). These parameters depend primarily on SME, with basically no dependence on the iterative analysis based on the *Hipparcos* parallax and YY isochrones (Section 3.1).

^b $Y^2+\text{Hip}+\text{SME}$ = YY isochrones (Yi et al. 2001), *Hipparcos* distance data, and SME results.

^c The distance given in the table is based on the self-consistent analysis that relies on the *Hipparcos* parallax and the YY isochrones. It slightly differs from the *Hipparcos*-based distance.

cross each other. Certain parameter combinations in the Monte Carlo search did not match any isochrone. In such cases ($\sim 14\%$ of all trials) we skipped to the next randomly drawn parameter set. At the end, we derived the mean values and uncertainties of the physical parameters based on their a posteriori distribution. We also refined the stellar surface gravity. The new value $\log g_{\star} = 4.59 \pm 0.03$ agrees well with the earlier SME value, and has much smaller uncertainty confirming our previous assumptions that the absolute magnitude for this star is a better luminosity indicator than the surface gravity.

We then repeated the SME analysis by fixing $\log g_{\star}$ to the new value, and only adjusting $T_{\text{eff}\star}$, $[\text{Fe}/\text{H}]$ and $v \sin i$. This second iteration yielded $T_{\text{eff}\star} = 4780 \pm 50$ K and $[\text{Fe}/\text{H}] = +0.31 \pm 0.05$. It also yielded $v \sin i = 0.3 \pm 0.5$ km s^{-1} , but for the same reason as given earlier we adopt the relaxed range $v \sin i = 1.5 \pm 1.5$ km s^{-1} . We accepted the above values as the final atmospheric parameters for this star. We then also repeated the isochrone search for stellar parameters, yielding $M_{\star} = 0.809^{+0.020}_{-0.027}$ M_{\odot} , $R_{\star} = 0.752 \pm 0.021$ R_{\odot} , and $L_{\star} =$

0.26 ± 0.02 L_{\odot} . Along with other stellar parameters, these are summarized in Table 4. The stellar evolutionary isochrones for metallicity $[\text{Fe}/\text{H}] = +0.31$ are plotted in the right panel of Figure 5, with the final choice of effective temperature $T_{\text{eff}\star}$ and the absolute magnitude M_K marked, and encircled by the 1σ and 2σ confidence ellipsoids.

The justification for our choice of using the parallax as the luminosity indicator is demonstrated by Figure 5. In the left panel, we plot a set of $[\text{Fe}/\text{H}] = +0.31$ Yale isochrones as a function of effective temperature, with the vertical axis being $\log g_{\star}$, and the observed values with their respective error ellipsoids overlaid. The middle panel shows the same set of isochrones with the a/R_{\star} luminosity indicator on the vertical scale. Here the geometric semimajor axis a/R_{\star} is determined from the photometric transit and RV data (as shown later in Section 3.2), and its error is significantly increased by the uncertainties in the eccentricity of the RV data. The right panel shows the same set of isochrones, with vertical axis being the absolute K magnitude. Overlaid is the observational constraint based on the apparent magnitude and *Hipparcos* parallax, along with the respective 1σ and 2σ error ellipsoids. It is clearly seen that the right panel imposes the tightest constraint on the stellar parameters. We note here that an isochrone search using the reported $J - K$ color (instead of $T_{\text{eff}\star}$ as color indicator) also agrees with the evolutionary models; however, the relative volume of its confidence ellipsoid is somewhat larger.

The effective temperature from the SME analysis and the surface gravity derived above correspond to a K4V star using Gray (1992). The $B - V$ color index from the YY isochrones is 1.063 ± 0.024 , also consistent with the K4 spectral type of Gray (1992). We also ran the Ramírez & Meléndez (2005) and Casagrande et al. (2006) temperature calibrations in reverse to back out the $B - V$ required to produce the SME temperature. We got $B - V = 1.025 \pm 0.023$ and 1.067 ± 0.025 , respectively. For the final value, we accepted their average: $B - V = 1.046 \pm 0.024$.

3.1.1. Baraffe Isochrones

We also investigated the dependence of stellar parameters on the choice of isochrones. Since HAT-P-11 is a K dwarf, we used the Baraffe et al. (1998) isochrones that are usually a better choice for late-type dwarfs. Baraffe et al. (1998) presented three sets of isochrones with different mixing length

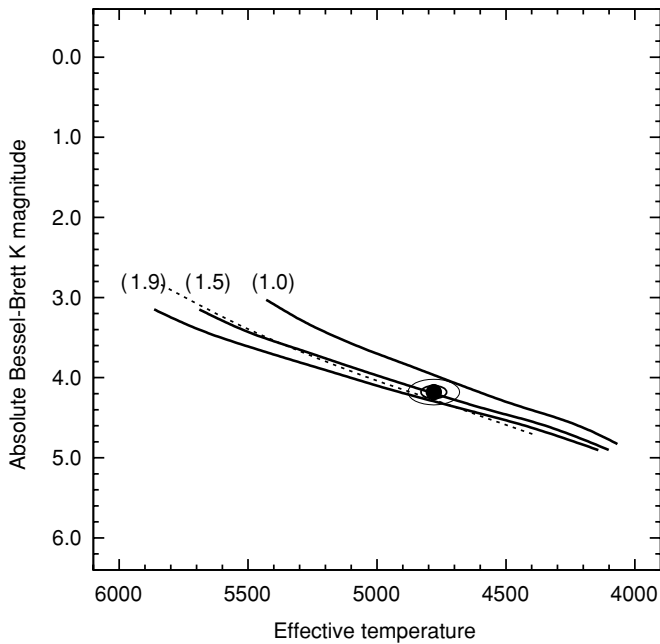


Figure 6. Baraffe et al. (1998) isochrones with mixing length parameters $\alpha = 1.0, 1.5,$ and 1.9 (solid lines) for solar metallicity (note that the metallicity of HAT-P-11 is $+0.31 \pm 0.05$). A metal-poor ($[\text{Fe}/\text{H}] = -0.3$) isochrone for $\alpha = 1.0$ from Baraffe et al. (1997) is overplotted as a dashed line to investigate the shift due to metallicity. Approximately the opposite shift can be expected when increasing the metallicity to $+0.31$, resulting in a mismatch between the observational values and the isochrones.

parameters. The one with $\alpha = 1.0$ is a better match for low-mass stars (such as late K or M dwarfs), the one with $\alpha = 1.9$ matches the Sun, and the third set with $\alpha = 1.5$ is in between. In Figure 6, we plot these isochrones as a function of $T_{\text{eff}\star}$, with the vertical axis being absolute K magnitude in the Bessel Brett system. Both the 2MASS K_s band and the Baraffe CIT systems were transformed to K using the relations in Carpenter (2001). The Baraffe isochrones for $\alpha > 1.0$ are given only for solar metallicity, while those for $\alpha = 1.0$ are available for solar and sub-solar (Baraffe et al. 1997) metallicity only, but not for the metal-rich composition of HAT-P-11 ($[\text{Fe}/\text{H}] = +0.31 \pm 0.05$). To investigate the effect of metallicity, we assumed the same qualitative behavior (i.e., opposite shift in the absolute magnitude–temperature plane) for isochrones with metallicity increased by $+0.3$, independent of their mixing lengths. In Figure 6, we overplot a metal-poor ($[\text{Fe}/\text{H}] = -0.3, \alpha = 1.0$) isochrone, and conclude that an opposite change in metallicity to match that of HAT-P-11 would move the $\alpha = 1.0, [\text{Fe}/\text{H}] = +0.3$ isochrone away from the observational values of K and $T_{\text{eff}\star}$. Because of the lack of metal-rich models from Baraffe, and the lack of the knowledge of the proper mixing length parameter, we omit any quantitative conclusions from these models. Altogether, we found a better match with the YY isochrones, and thus accepted YY-based stellar parameters as final values (Table 4).

3.2. Constraints on Stellar Parameters by the Normalized Semimajor Axis

As noted by Sozzetti et al. (2007) and Torres et al. (2008), a possible luminosity indicator for host stars of transiting planets is the a/R_\star quantity, where a is the relative semimajor axis, and R_\star is the radius of the host star. Here a/R_\star is in simple relation with the mean stellar density, if we assume that the planetary

mass is much smaller than the stellar mass:

$$\rho_\star = 0.01892 \frac{(a/R_\star)^3}{(P/\text{day})^2} \text{ g cm}^{-3}. \quad (1)$$

Analysis of the transit light curve yields—among other parameters—the quantity ζ/R_\star that is related to the time spent in between the planetary center crossing the limb of the star as $T_{\text{dur}} = (2\zeta/R_\star)^{-1}$. For circular orbits and equatorial transits a/R_\star is a function of ζ/R_\star and the orbital period, and thus can be determined in a straightforward way. For eccentric orbits, the relation between ζ/R_\star and a/R_\star , as based on Tingley & Sackett (2005):

$$\frac{\zeta}{R_\star} = \frac{a}{R_\star} \frac{2\pi}{P} \frac{1}{\sqrt{1-b^2}} \frac{1+h}{\sqrt{1-e^2}}. \quad (2)$$

Thus, in addition to the light-curve parameters, a/R_\star also depends on the orbital eccentricity and argument of pericenter, and uncertainties in these parameters propagate into the error of a/R_\star .

In the case of HAT-P-11, the RV data show a significant eccentricity of $e = 0.198 \pm 0.046$ (Section 5). Although ζ/R_\star and the $\sqrt{1-b^2}$ terms have small uncertainties (1.0% and 4.8%, respectively), the uncertainty in the $(1+h)/\sqrt{1-e^2}$ term is higher, yielding a final value of $a/R_\star = 14.6_{-1.4}^{+1.7}$. The significant error can be credited to the uncertainties in the orbital parameters, as caused by the small RV amplitude and the stellar jitter. For comparison, if a/R_\star is calculated backward from the *Hipparcos*-parallax-based stellar evolutionary modeling, we get $a/R_\star = 15.58_{-0.82}^{+0.17}$. It is reassuring that this is consistent with that derived from the global modeling of the data, but the uncertainties are ~ 3 – 4 times smaller. This justifies the choice of the *Hipparcos*-parallax-based luminosity indicator over using the a/R_\star constraint from global modeling of the data. This is also confirmed by comparing panels (b) and (c) of Figure 5, where the confidence ellipsoids from the parallax constraint (panel c) impose a tighter constraint on the isochrones.

3.3. Rotation and Activity of HAT-P-11

The EPD (pre-TFA) HATNet light curve of HAT-P-11 shows significant periodic variations with $P \approx 29.2$ days and a peak-to-peak amplitude of 6.4 mmag in I -band (Figure 7). This period is detected both in the autocorrelation function and the Fourier power spectrum of the light curve. The period is detected in both seasons covered by the HATNet light curve, and the signal remains in phase across both seasons as well. While this period is suspiciously close to the lunar cycle, we note that the light curve is relatively unchanged by the EPD procedure, i.e., these variations do not appear to correlate with any external parameters, including the sky background. The TFA procedure does suppress this signal when several hundred template stars are used. However, this is often the case when applying non-reconstructive TFA to other long-period variable stars such as Cepheids or Miras. To test whether or not this signal is due to some non-astrophysical systematic variation, we searched for other light curves exhibiting a strong peak in the Fourier power spectrum near $f = 0.034$ [c/d]. We found that nine out of the 5000 brightest stars with $I \lesssim 10.0$ showed such a peak; however, none of these stars are in phase with HAT-P-11. Moreover, the distribution of peak frequencies does not show a pile-up at $f = 1/P = 0.034 \text{ day}^{-1}$ relative to other frequencies, which one might expect to see if this variation were a systematic trend. As a final test, we attempted to recover the signal after applying

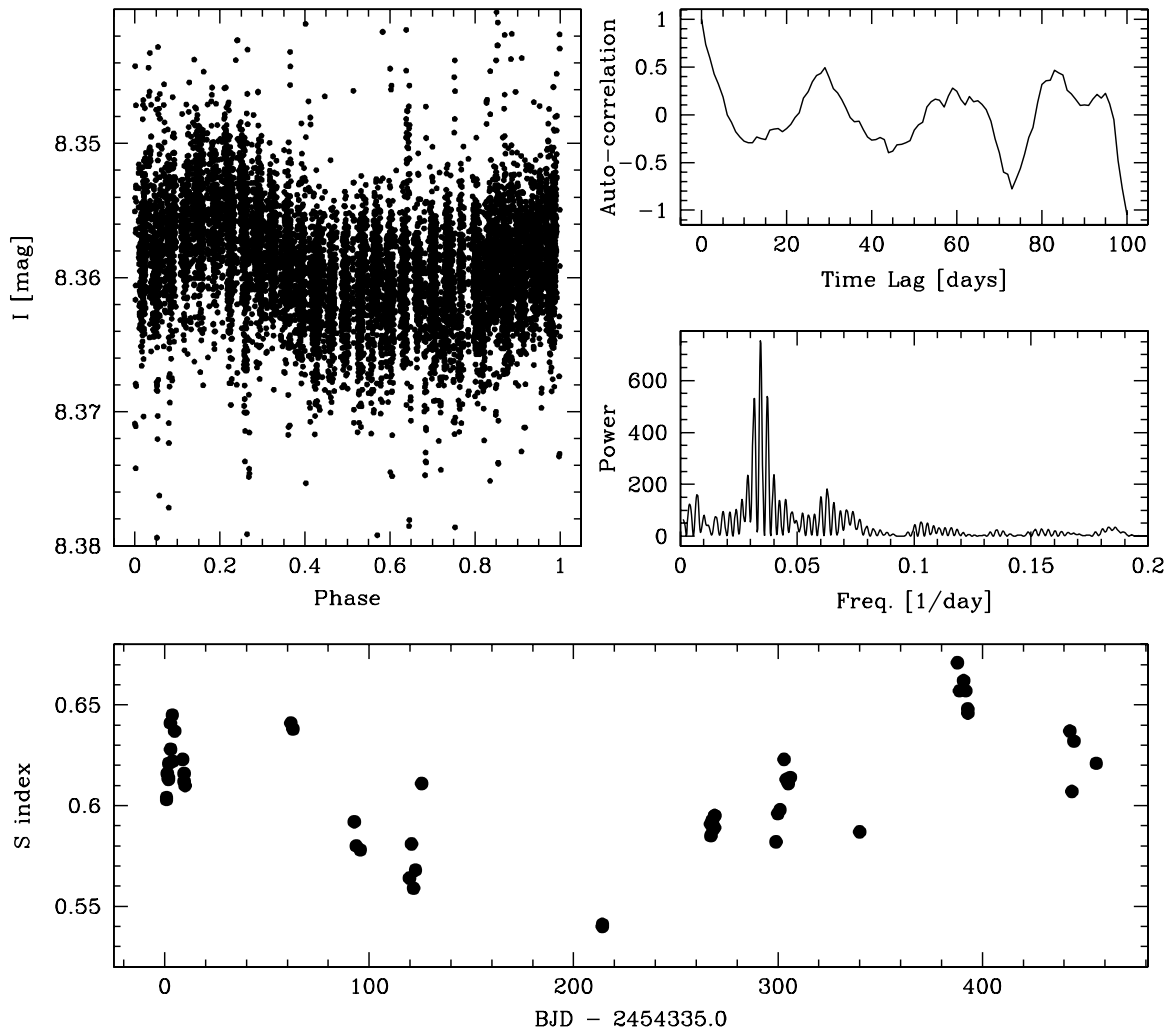


Figure 7. Left: pre-TFA, post-EPD HATnet I -band light curve of HAT-P-11 phased at a period of $P = 29.2$ days. Only OOT points are included in this plot. The apparent 6.4 mmag peak-to-peak variation may be due to the rotational modulation of starspots on the surface of HAT-P-11. Upper right: the autocorrelation function of the light curve at left. Note the first peak at a time lag of 29 days. Middle right: the Lomb-Scargle periodogram of the light curve at left. Note the peak at a frequency of 0.034 days^{-1} . Bottom: the S -index as a function of time. Note the long-term variations in the stellar activity.

different TFA template sets. We tried 100 disjoint template sets of 140 light curves. In all cases, the $P \approx 29.2$ day signal was recovered in the autocorrelation function. We conclude that the signal is not a systematic variation that is present in the light curves of many other stars, and if it is not of astrophysical origin then it is due to a phenomenon that affects the light curve of HAT-P-11 in an apparently unique manner.

A likely interpretation of the variation seen in Figure 7 is that it is due to the rotational modulation of starspots on the surface of HAT-P-11. The 6.4 mmag amplitude of the variation is consistent with other observations of spotted K dwarf stars. Note that there is no significant $f_2 = 0.034 \text{ [c/d]}$ periodicity in the RV data, when it is modeled as the combination of a Keplerian orbit plus a sinusoid component (see Figure 3). The secondary peaks in the autocorrelation function in the figure, plus the co-phasing of the 29 day variation over two observing seasons (left curve of Figure 7) indicate that individual starspots or starspot groups persist for at least several rotations.

If the variation is indeed due to rotational modulation by starspots, then the rotation period of HAT-P-11 is $P \approx 29.2$ days. This may be compared with the rotation period predicted from the $B - V$ color of the star and the Ca II emission index S , using relations of Noyes et al. (1984). From Table 3,

the median value of S observed from HIRES is $\langle S \rangle = 0.61$. This value and $B - V = 1.046 \pm 0.024$ as derived earlier yield a rotation period of $P_{\text{calc}} = 24.2$ days. The uncertainty in this calculation is difficult to quantify. The relations given in Noyes et al. (1984) were based on a theoretically motivated fit to the rotation period determined for a number of lower main-sequence stars from the rotational modulation of their chromospheric emission. For the 18 K stars in their sample with measured rotation periods P_{obs} , the rms difference between P_{obs} and the calculated value P_{calc} is 3.5 days. However, Noyes et al. (1984) pointed out that the empirical relation for P_{calc} as a function of S and $B - V$ becomes rather unreliable for $B - V \gtrsim 1.0$, because of a paucity of stars with observed rotation periods in this color range. Hence, the true uncertainty is doubtless somewhat larger than 3.5 days. We conclude that a rotation period of 29.2 days is consistent with expectations from the star's $B - V$ color and $\langle S \rangle$ value.

A 29 day rotation period of HAT-P-11, coupled with its radius, implies an equatorial velocity $v_{\text{eq}} = 1.3 \text{ km s}^{-1}$. Let us assume that the stellar rotational axis is inclined at $i \sim 90^\circ$ to the line of sight. This is supported by the geometry of our solar system and the generally similar geometries of the stellar systems with transiting planets whose projected rotational axis inclinations

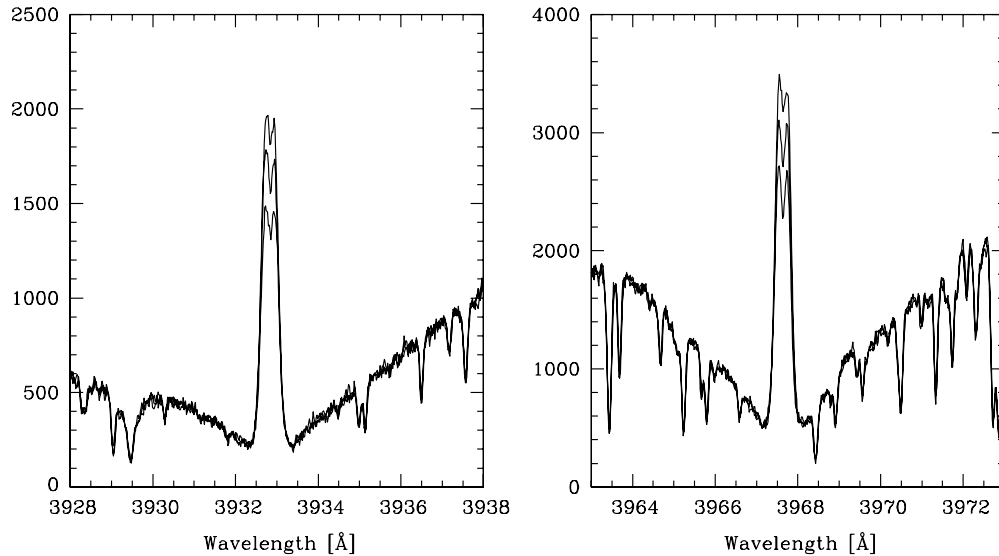


Figure 8. Calcium K (left) and H (right) line profile in selected HIRES observations of HAT-P-11. Both panels show three spectra overlaid; data taken at high, median, and low activity, as characterized by the S index. The spectra are matched to a common flux/wavelength scale using points outside the H and K line cores. The vertical axes on the plots are arbitrary and proportional to counts.

have been measured through the Rossiter–McLaughlin effect. We would then expect $v \sin i \sim 1.3 \text{ km s}^{-1}$, consistent with the value of $v \sin i$ reported in Table 4.

Figure 7 shows the time history of the Ca II S index. Figure 8 shows the very prominent emission cores of the Ca II H and K lines observed at three levels of activity during the time of the HIRES observations. A long-term variation of S is apparent, with timescale close to the length of the current data set. As discussed later, this may be due to long-term variations of stellar activity analogous to the solar activity cycle. Phasing of the S data at a period of 29.2 days shows no evidence for periodic behavior. If the star is really rotating at a period of 29 days, this suggests that the chromospheric emission in the H and K lines is spread nearly uniformly in longitude over the star.

The color $B - V = 1.046$ of HAT-P-11 and its median level of chromospheric emission $\langle S \rangle = 0.61$ imply a chromospheric emission ratio R'_{HK} given by $\log R'_{HK} = -4.584$ (Noyes et al. 1984). From this, we may crudely estimate an age for the star using the inverse square root relation between activity and age as originally posited by Skumanich (1972). Using a fit of this relation to the Sun, the Hyades, the Ursa Major group, and 412 individual lower main-sequence stars as derived by Soderblom et al. (1991), we determine a “chromospheric age” $T_{\text{cr}} \sim 1.25 \text{ Gyr}$. The uncertainty in this estimate is difficult to quantify, especially because most of the stars in the sample had $B - V < 1.0$, but it does suggest that based on its chromospheric emission level the star is likely to be at the low end of the age range given in the isochrone fit discussed in Section 3.1.

4. EXCLUDING BLEND SCENARIOS

4.1. Spectral Line-bisector Analysis

As always in determining whether the signature from combined photometric and RV variations in a star is due to a transiting planet, it is necessary to exclude the possibility that the entire combined information is due to a set of circumstances that falsely give rise to the characteristic signature of a transiting planet. Following Torres et al. (2007), we first explored the possibility that the measured RV variations are caused by distortions in the spectral line profiles due to a nearby unresolved

faint eclipsing binary, whose relatively large RV variations mix with the non-varying spectrum of the primary and give rise to an apparent RV signal with the observed small amplitude. In this case it has been shown (e.g., Queloz et al. 2001) that the BS of spectral lines in the blended spectrum varies in phase with the RV signal itself, with similar amplitude. We have carried out an analysis of the BS based on the Keck spectra as described in earlier HATNet detection papers (see Bakos et al. 2007), and do not see any statistically significant correlation between the line BSs and the measured radial velocities (confer Figure 4 and Table 3), thus providing no support for the hypothesis that the signal is caused by a blended eclipsing stellar system.

However, because of the small amplitude of the RV signal (and hence small amplitude of expected BS variations if the apparent RV signal is indeed due to a blend), coupled with the large jitter as seen in the RV residuals in Figure 4, the above test cannot completely rule out contamination by an unresolved binary system. Thus, we sought other independent ways of excluding blend scenarios. In the following subsections, we attempt to model the system as a hierarchical triple, where the smallest component is either a star or a Jupiter-sized planet, and also as a background eclipsing binary blended with the light of a foreground K dwarf. We show that none of these models are consistent with all of the available observations.

4.2. Detailed Blend Modeling of a Hierarchical Triple

We consider the possibility that HAT-P-11 is a hierarchical triple system, having a deeper intrinsic eclipse of two bodies diluted by the light of the bright K dwarf. Note that the bright K dwarf with well known properties (parallax, proper motion, etc.) in this putative triple system is referred to as HAT-P-11 in the following discussion. To rule out the hierarchical triple scenario, we attempt to fit a blend model to the observations. There are two scenarios for the eclipsing system in the triple system. The first one is a stellar eclipsing binary. The second case is a transiting hot Jupiter orbiting a low-mass star, with the few percent deep transit diluted by HAT-P-11 to become only 4.2 mmag. We note that the shallower the transit event, the larger the variety of configurations that can match the observations. HAT-P-11

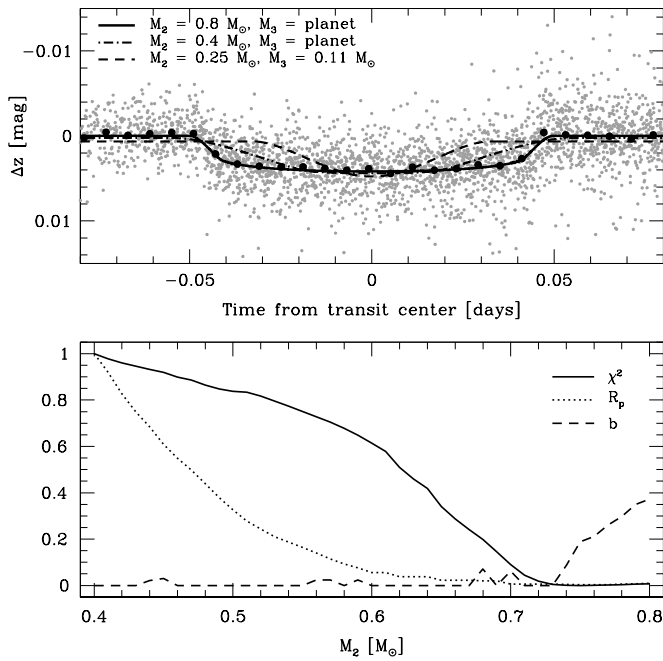


Figure 9. Top: z -band follow-up light curve for HAT-P-11 with model light curves for three blend models overplotted. The dark points show the binned light curve, while the light points show the unbinned light curve. The solid line shows a model where a planet orbits one component of a binary star, with the planet-hosting star having a mass of $0.8 M_{\odot}$. The dot-dashed line shows a similar scenario but where the planet-hosting star has a mass of $0.4 M_{\odot}$. The dashed line shows the best-fit hierarchical triple model consisting of eclipsing binary star system bound to a distant third star. We can rule out the hierarchical triple scenario and the blend models where a planet orbits a binary star component that is smaller than $0.72 M_{\odot}$, blend scenarios with a larger planet-hosting star can fit the light curve but a second star this massive would have been detected in the Keck and DS spectra. Bottom: here we show χ^2 , the planet radius R_p and the impact parameter b as a function of the planet-hosting star mass for the blend scenario of a planet orbiting one component of a binary system. χ^2 is linearly scaled between 95,788 and 100,457, while R_p is linearly scaled between $0.583 R_J$ and $2.17 R_J$. For stellar masses below $0.72 M_{\odot}$, the planet radius needed to fit the transit depth and duration yields an ingress and egress time that is too long. Above $0.72 M_{\odot}$ the impact parameter increases to fit the transit duration, while the planet radius needed to fit the transit depth changes slowly.

represents a transition toward millimag transit events, the blend analysis of which will certainly be challenging.

In each case (stellar binary, versus transiting hot Jupiter blend), we fit the follow-up z , r , and I_C -band light curves together with the HATNet I -band light curve following a procedure similar to that described by Torres et al. (2005). We assume that the bright star (HAT-P-11), which is not eclipsed, has the mass, metallicity, age, and distance determined in Section 3. We also assume the components of the eclipsing system have the same metallicity, age, and distance as the bright star, i.e., they form a hierarchical triple. We fix the ephemeris, orbital eccentricity, and argument of periastron to the values determined in Section 5.4, and vary the masses of the two components and the inclination of the orbit. The downhill simplex algorithm is used to optimize the free parameters. For the case where one of the components is a planet, we vary the radius of the planet rather than its mass. For the eclipsing binary case, the magnitudes and radii of the stars are taken from the Padova isochrones (Girardi et al. 2000) applying the radius correction described by Torres et al. (2005). We use these isochrones to allow for stars smaller than $0.4 M_{\odot}$. For the planet case, we use the YY isochrones to be consistent with the single-star planet modeling.

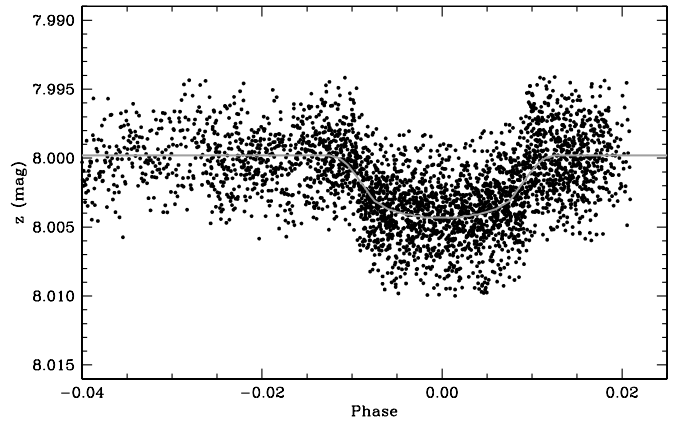


Figure 10. Sample blend model fitted to our combined z -band measurements (arbitrary scale on the vertical axis). The solid line represents the light curve resulting from a background eclipsing binary system whose flux is diluted by the main star, which contributes 95% of the z -band light in this case. The eclipsing binary is composed of $0.64 M_{\odot}$ and $0.13 M_{\odot}$ stars in an edge-on configuration, placed 60 pc behind the target. The predicted relative brightness of the primary in this scenario is only 3% of the light of the main star in the optical.

Figure 9 shows the best-fit model for the eclipsing binary case and two illustrative models for the blended hot-Jupiter case overplotted on the z -band light curve. We are unable to fit the light curve using a combination of three, physically associated stars, but are able to fit it as a planet transiting one component of a binary star system, so long as the star hosting the planet has $M > 0.72 M_{\odot}$. Interestingly, $0.72 M_{\odot}$ emerges as a critical mass (and corresponding critical radius, luminosity) for the eclipsed star, and splits the parameter space into two disjoint domains. As the mass of the host star is reduced below $0.72 M_{\odot}$ (and its radius is decreased), the only way to maintain the depth and duration of the already central ($b = 0$, i.e., longest possible) transit is to increase the radius of the planet. This, however results in a longer ingress and egress time than is allowed by the observations. Above $0.72 M_{\odot}$ the radius of the planet needed to fit the transit depth changes slowly, while raising the impact parameter of the planet can compensate to fit the transit duration (see Figure 9). While a model of this form fits the light curve, the V -band light ratio of the planet-hosting star to the brighter $0.81 M_{\odot}$ star would be > 0.46 . The spectrum of a second star this bright should have been easily detected in the Keck and DS observations, and therefore we can rule out both of these blend scenarios.

4.3. Contamination from a Background Eclipsing Binary

An alternate model of an astrophysical false positive that would make the contaminating star much fainter relative to the main object is one involving a background eclipsing binary (chance alignment). We modeled this case using the same methodology described above, fitting the combined z -band follow-up light curves as the sum of the light from three stars. The properties of the main star were held fixed as before, and those of the eclipsing binary components were constrained to lie on the same isochrone, which for simplicity was taken to be the same as the main star. Extensive tests indicated that the detailed shape of the resulting synthetic light curve is fairly insensitive to the distance at which we place the eclipsing binary behind the target, and thus acceptably good fits to our z -band photometry can be achieved for a wide range of distances, given the measurement precision. Figure 10 shows an example of such a fit, in which the eclipsing binary is placed about 60 pc

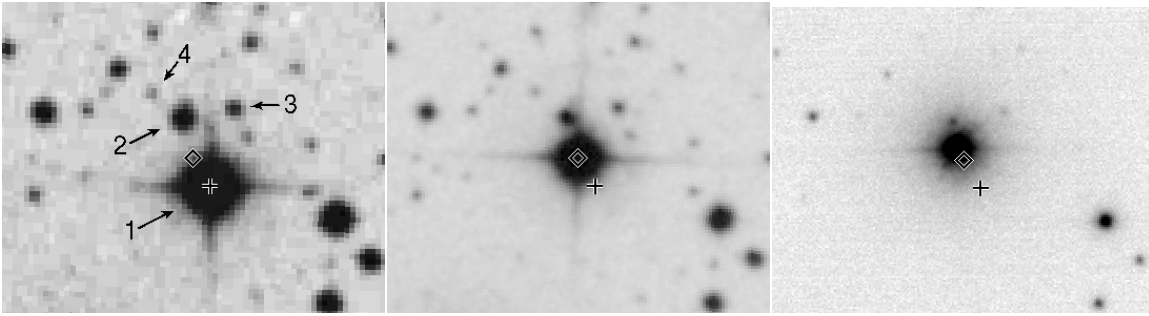


Figure 11. Images of a $2' \times 1.7'$ field containing HAT-P-11 from the POSS-I Red survey (left), POSS-II Red survey (center), and a FLWO 1.2 m z -band image (right; see Section 2.3). The dates of the exposures are 1951 July 10, 1989 August 25, and 2007 September 2, respectively. The cross marks the position of HAT-P-11 in the POSS-I image (labeled as star 1), while the diamond marks the position of HAT-P-11 in the POSS-II image. Between 1951 and 2007 HTR155-001 moved $13''.8$ in the north–northeast direction. Stars labeled 1 through 4 on the POSS-I image have USNO A-2.0 R magnitudes of 10.8, 15.1, 17.2, and 18.9, respectively (USNO-A2.0; Monet 1998). From the POSS-I image, we can rule out stars brighter than $R \sim 19$ at the current position of HAT-P-11.

behind the main star and is composed of a $0.64 M_{\odot}$ star (spectral type K7V–M0V) orbited by a $0.13 M_{\odot}$ stellar companion. This model is not only consistent with the photometry, but it predicts an optical brightness for the primary of the eclipsing binary of only 3% relative to the main star. Detecting such a faint set of spectral lines in our Keck spectra would be challenging. Furthermore, if we place the eclipsing pair 110 pc behind the main star, the light curve fit is still about the same, but the relative brightness decreases by a factor of 2, making the eclipsing binary spectroscopically undetectable. Spectral line bisector variations predicted by this second model (see, e.g., Torres et al. 2005) would be at the level of the scatter in our actual measurements, and thus could not be entirely ruled out either.

While this blend scenario appears to satisfy all observations, it implies the presence of an eclipsing binary ~ 4.5 mag fainter in the optical very near the present location of our target. It is fortunate that HAT-P-11 has a large proper motion ($0''.264 \text{ yr}^{-1}$; Perryman et al. 1997). Using Palomar Observatory Sky Survey plates from 1951 (POSS-I, red and blue plates), we can view the sky at the current position of HAT-P-11 *unobstructed*, since the target was $15''$ away. Figure 11 shows a stamp from the POSS-I, POSS-II plates, and also a current observation with the FLWO 1.2 m telescope. The proper motion of HAT-P-11 is apparent. A number of faint stars are marked on the figure. Note that the faintest possible star that can cause the observed 4.2 mmag variation in the combined light curve would be 6 magnitudes fainter than HAT-P-11, and in this extreme situation the blended faint star would need to completely disappear during its transit. There is no faint star down to ~ 19 mag within $\sim 5''$ of the current position of HAT-P-11. The closest star marked “2” in Figure 11 is 2MASS 19505049+4805017, with $z \approx 14.4$, or about $z \approx 5.6$ mag fainter than HAT-P-11. This is well resolved in some of our follow-up photometry observations, such as on the 2007 September 2 night, and its brightness was constant, with rms much smaller than the required amplitude of its variation should be (~ 1.3 mag) to cause the observed 4.2 mmag combined dip.

In summary, we (1) have not seen bisector variations correlated with the RV, (2) investigated unresolvable hierarchical triple systems (blended eclipsing binary or transiting hot Jupiter), and found all to be incompatible with the photometric and spectroscopic data together, and (3) were able to exclude chance alignment of a background eclipsing binary based on the high proper motion of the star. We therefore conclude that the transit signal, and the synchronized RV signal, indeed are both due to a sub-stellar companion transiting the K4 dwarf HAT-P-11.

5. GLOBAL MODELING OF THE DATA

In order to perform an optimal analysis of the data at hand, we assembled a global model of a planetary transit scenario that describes all the data components: (1) the HATNet discovery light curve, (2) the photometric follow-up light curves of 10 independent events, and (3) the RV data from Keck (Section 5.1). The physical model was then extended by a model that describes systematic variations in the data (Section 5.2). We then performed a joint fit of the combined physical plus systematic model by using all these data simultaneously to derive the physical parameters, and also to correct for the systematic variations (Section 5.3). The results are discussed in Sections 5.4 and 5.5.

5.1. Physical Model for the Light Curve and Radial Velocity

Our model for the follow-up light curves used analytic formulae based on Mandel & Agol (2002) for the eclipse of a star by a planet, where the stellar flux is described by quadratic limb darkening. We did not attempt to fit for the limb-darkening coefficients, as they require very high quality data to resolve their degeneracy with other parameters. Instead, the limb-darkening coefficients were derived from the second iteration SME results (Section 3), using the tables provided by Claret (2004) for z , r (FLWO 1.2 m), and I_C bands (Konkoly 0.6 m Schmidt). The transit shape was parameterized by the normalized planetary radius $p \equiv R_p/R_*$, the square of the impact parameter b^2 , and the reciprocal of the half duration of the transit¹⁶ ζ/R_* . We chose these parameters because of their simple geometric meanings and the fact that these show negligible correlations (see Carter et al. 2008; Bakos et al. 2007; Pál 2008b).

Our model for the HATNet data was a simplified version of the Mandel & Agol (2002) analytic functions, because (1) the number of in-transit data points in the HATNet light curve is significantly less than the same number for the follow-up light curves, and (2) the individual errors on the points are much worse for HATNet than for the follow-up. Thus, while the HATNet data are efficient in constraining the ephemeris, they are not comparable to the follow-up data in determining other transit parameters that depend on the exact shape of the transit (such as depth, or duration of ingress). For these reasons, we employed a simple transit model that neglects limb

¹⁶ The duration is defined as the time between the contact centers, i.e., when the center of the planetary disk crosses the limb of the star during ingress and egress.

darkening. This model function, which we label as “PIP3,” originates from an expansion of the exact Mandel & Agol (2002) model function by Legendre polynomials, resulting in a functional form (omitting scaling factors) of the ingress (and symmetrically, the egress) of $x \rightarrow (21x - 5x^3)/16$, where the independent variable x is scaled to be 1 at first (third) contact, and -1 at second (fourth) contact. For reference, the trapeze model has a simple linear function describing the ingress: $x \rightarrow x$. The “PIP3” model approximates the Mandel & Agol (2002) function to better than 1%, and our experience shows that such an approximation yields the same timing precision as more sophisticated model functions. In addition, using the simplified model yields much faster computation. A similar transit model approximation using hyperbolic tangent functions was described earlier by Protopapas et al. (2005). The depth of the HATNet transits was also adjusted in the fit (independent of the follow-up data), and we found that the depth derived from the HATNet light curve is comparable (Section 5.4) to the depth of the (EPD and TFA reconstructed) follow-up transit measurements, namely, the ratio of the two was $B_{\text{inst}} = 0.95 \pm 0.08$. In general, this “instrumental blend” parameter has to be adjusted independently since the possible contamination by nearby stars in the wide-field images may yield shallower transits.

The adopted model for the RV variations was described earlier in Section 2.4. The RV curve was parameterized by an eccentric Keplerian orbit with semi-amplitude K , RV zero-point γ , Lagrangian orbital elements $(k, h) = e \times (\cos \omega, \sin \omega)$, plus a linear trend G_1 .

We assumed that there is a strict periodicity in the individual transit times. In practice, we introduced the first transit center as $T_A = T_{c,-231}$ and the last transit center as $T_B = T_{c,+91}$, covering all of our measurements with the HATNet telescopes, the FLWO 1.2 m telescope and the Schmidt telescope. The transit center times for the intermediate transits were interpolated using these two epochs and the N_{tr} transit number of the actual event under the assumption of no transit timing variations (TTVs). The model for the RV data contained the ephemeris information through the $T_{c,-231}$ and $T_{c,+91}$ variables; for instance, the period assumed during the fit was $P = (T_{c,+91} - T_{c,-231})/(91+231)$. The other coupling between the transit photometry and the RV data is via the k and h Lagrangian orbital elements that determine the relation between the photometric and orbital ephemeris, plus have a minor effect on the transit shape. Altogether, the 12 parameters describing the physical model were $T_{c,-231}$, $T_{c,+91}$, R_p/R_* , b^2 , ζ/R_* , K , γ , $k = e \cos \omega$, $h = e \sin \omega$, and G_1 . As mentioned above, the parameters were extended with the instrumental blend factor B_{inst} , and the HATNet out-of-transit (OOT) magnitude, $M_{0,\text{HATNet}}$.

5.2. Models for Systematic Variations

A “joint” fit of the physical model to the global data set has been performed routinely for recent discoveries (Bakos et al. 2009; Latham et al. 2009). Here we extended our physical model that describes the transit events and the radial velocities with an instrumental model that describes the systematic variations of the data. Since the HATNet photometry has been already EPD and TFA corrected (Section 2.1), and the Keck RVs have been investigated for trends (Section 2.4), but deemed to have insufficient number to decipher any significant systematic variation (50 points compared to $\mathcal{O}(10^4)$ points for photometry), we only modeled systematic variations of the follow-up photometry (Section 2.3). As mentioned earlier, the effect of systematics

on the shallow transit in the photometric follow-up data is enhanced, and can impact the basic planetary parameters, such as the planetary radius. We experimented with several models, since the treatment of systematics may improve precision, but not necessarily the accuracy of the results. For reference, we call the simplest model, with no EPD and no TFA, as model “EOTO” (for technical details, see the Appendix).

Model “EOTRG” was independent (i.e., not simultaneous) reconstructive global TFA of the FLWO 1.2 m z -band data (eight nights, see Table 1), assuming a trapeze-shaped $m_0(\vec{p}, t)$ model function in Equation (A2) with three parameters (total duration, ingress duration, and depth). The period was iteratively refined using both the FLWO 1.2 m and the HATNet data, but reconstructive TFA was only performed on the FLWO photometry. We used the magnitude values transformed to the selected reference frame for each night (see Section 2.3), and the zero-point shift for each night was determined separately. We increased the number of template stars till the S/N of the trapeze reached its maximum (S/N = 39), requiring 246 stars with $z \lesssim 14$. Note that this was a global TFA, in the sense that there was one c_k TFA coefficient per star in Equation (A3) for all nights combined (see Appendix A.2). The reconstructed light curve was then fed into the joint fit.

Model “ELT0” had EPD parameters in the simultaneous fit, together with the parameters of the physical model, but no TFA-based detrending, i.e., all the systematic variations in the follow-up photometry were modeled as due to external parameters. We chose five such parameters, namely the hour angle (characterizing a monotonic trend that linearly changes over time), the square of the hour angle, the stellar profile sharpness parameter, $S = (2.35/\text{FWHM})^2$, the X and Y pixel position on the chip (each with two coefficients). The exact functional form of the above parameters contained eight coefficients, including the auxiliary OOT magnitude of the individual events. The EPD parameters were independent for all 10 nights, implying 80 additional coefficients in the global fit.

Model “EOTL” had local TFA parameters in the instrumental model for each night, and no EPD was used. We selected 23 TFA template stars that were present in all observations, representing faint and bright stars spread across the chip. The total number of c_k coefficients in the simultaneous fit was thus 230. Model “EOTG” had global TFA parameters for all nights, using 211 stars that were present on all frames. Note that without simultaneous fit using an underlying physical model ($m_j(t_i)$) in Equation (A2)) that takes into account the different shape of the light curves acquired through different photometric bands, such a global TFA fit would not be possible.

We tested variants of the above methods. Model “ELTL” was a simultaneous fit of EPD and TFA parameters in local EPD mode and local TFA mode with altogether 80 + 230 parameters in addition to the 12 physical parameters. Model “ELTG” was a simultaneous fit of local EPD and global TFA parameters with an additional 80 + 211 instrumental parameters. The parameter sets were extended in all cases with the OOT magnitudes for each follow-up light curve and the HATNet photometry. The number of fitted parameters was much smaller than the number of data points (~ 5000).

5.3. Performing the Joint Fit

It is computationally rather intensive to perform a fit with ~ 300 parameters and to determine their respective error distributions.

Table 5
Light Curve Parameters Involving Different Kinds of Models for Systematic Variations

Method	$T_{c,+91} - 2454790.0$	R_p/R_*	b^2	ζ/R_*
EOTO ^a	1.62781 ± 0.00055	0.06035 ± 0.00140	0.165 ± 0.120	22.05 ± 0.24
EOTL ^b	1.62793 ± 0.00047	0.05831 ± 0.00094	0.114 ± 0.087	21.82 ± 0.18
EOTG ^c	1.62772 ± 0.00046	0.05730 ± 0.00096	0.112 ± 0.091	21.99 ± 0.19
EOTRG ^d	1.62758 ± 0.00133	0.05690 ± 0.00150	0.223 ± 0.137	22.10 ± 0.27
ELTO ^e	1.62834 ± 0.00044	0.05825 ± 0.00094	0.109 ± 0.093	22.25 ± 0.17
ELTL ^f	1.62826 ± 0.00040	0.05675 ± 0.00097	0.113 ± 0.093	22.17 ± 0.16
ELTG ^g	1.62832 ± 0.00039	0.05758 ± 0.00091	0.120 ± 0.087	22.15 ± 0.15

Notes.

^a No EPD and no TFA performed on the photometric follow-up data.

^b No EPD, and per night “local” TFA performed with 23 TFA template stars and simultaneous fitting with the transit model.

^c No EPD, and global simultaneous TFA performed with 211 TFA templates.

^d No EPD. Global reconstructive trapeze TFA performed with 246 TFA templates. Only the eight nights of FLWO z -band observations were used.

^e EPD performed using five free parameters per night. No TFA.

^f EPD as for ELTO. TFA as for EOTL.

^g EPD as for ELTO. TFA as for EOTG.

Since the majority of the fitted parameters appear as linear terms in the final form of the model functions, we minimized χ^2 in the parameter space by using a hybrid algorithm, namely, by combining the downhill simplex method (aka AMOEBA; see Press et al. 1992) with the classical linear least-squares (CLS) algorithm. The simplex itself was propagating in the “nonlinear” hyperplane of the parameter space, while in each point of the hyperplane the value of χ^2 was computed using classical linear CLS minimization. This method yielded a very good convergence even with the large number of free parameters.

Uncertainties of the parameters were derived using the Markov Chain Monte Carlo method (MCMC; see Ford 2006) by starting two types of chains from the best-fit value. The first one was the classical MCMC chain, letting all parameters vary. The other type of chain was generated by only allowing the variation in a hyperplane of the parameter space consisting of the nonlinear parameters and of some additional linear parameters where error calculation was desired (examples are K , γ or G_1). In this “Hyperplane-CLS” chain, the remaining linear parameters were determined at each step via CLS. The H-CLS chain has the advantage that transition probabilities are much higher in the separated hyperplane, and thus the convergence and computing time requirements are also smaller by an order of magnitude. Furthermore, the error distribution of parameters for the hyperplane variables was identical to those determined by classical MCMC. The distribution for the parameters outside the hyperplane was distorted, but these were considered as auxiliary, where such distribution is irrelevant (e.g., the EPD and TFA coefficients). Therefore, the final distribution of the physical parameters was derived by using H-CLS chains.

For both types of the chains the a priori distributions of the parameters were chosen from a generic Gaussian distribution, with eigenvalues and eigenvectors derived from the Fisher covariance matrix for the best-fit value. All functions that appear in the physical and instrumental model are analytical, and their partial derivatives are known. The parametric derivatives of the transit light-curve model of Mandel & Agol (2002) are found in Pál (2008b), while the parametric derivatives of the eccentric RV curves can be obtained by involving the implicit function theorem, and can be expressed as functions of the eccentric

anomaly. Thanks to these analytic properties, the derivation of the Fisher matrix was straightforward.

5.4. Results of the Fit and the Effect of Systematics

We performed a joint fit on the HATNet light curve, the follow-up photometry, and the Keck radial velocities (the “data”), using the physical model described in Section 5.1, as extended by the various models for systematics (Section 5.2), and using the algorithms described in Section 5.3.

We carried out the fit considering each model describing the systematics in the follow-up photometry separately in order to investigate their effect on the final results. As mentioned earlier, this is important due to the very shallow transit signal and the large relative amplitude of systematic variations. We used the m_f -fitted magnitude values (Section 2.1) for the photometry follow-up light curves (without prior EPD or TFA). Since only the follow-up photometric data component was described by the different systematic models (see Section 5.2), we focused on those light-curve parameters that are affected by the photometric follow-up, namely, the transit center time of the last event $T_{c,+91}$, the radius ratio of the planet to star, the (square of the) impact parameter and the transit duration parameter ζ/R_* . The other adjusted parameters were not relevant in this comparison, since they are not affected by the follow-up light curves. Note that with the exception of the EOTRG model, all EPD and TFA parameters were fit *simultaneously* with the physical model parameters.

The best-fit values and the respective uncertainties are summarized in Table 5. It is clear that EPD and TFA both significantly reduce the uncertainties in all the parameters. Note that the implementation of EOTRG was somewhat sub-optimal. Because the reconstructive trapeze shape was not bandpass dependent (as opposed to the full Mandel & Agol (2002) model used in the other cases), only a fraction of the follow-up were used, namely, all photometry in z band. When using EPD and TFA together, the global TFA (ELTG) performs better than local TFA (ELTL) for each night. The improvements by EPD (ELTO) and TFA (EOTG) separately are roughly the same. The best model, based on the formal error bars, is the EPD and global TFA together (ELTG); here the unbiased error in the light-curve parameters decreased by a factor of 1.5.

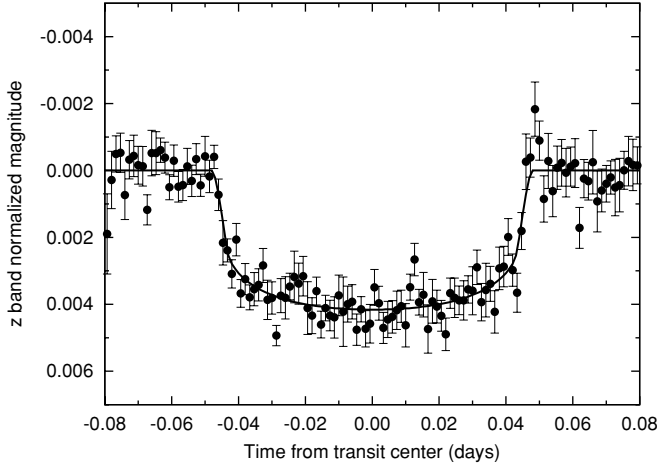


Figure 12. Combined and binned light curve of HAT-P-11, involving all the z -band photometry, obtained by KeplerCam. The light curve is superimposed with the best-fit model (which is the result of the joint fit described in Section 5).

The final value for the parameters also changed by 3σ in the sense that both R_p/R_* and b^2 decreased. This means that the treatment of the systematics recovers a sharper transit with smaller impact parameter and smaller planetary radius. If the stellar parameters were determined using the a/R_* luminosity constraint (Section 3.2), then ignoring the correction for systematics would lead to higher impact parameter, larger R_p/R_* , and smaller a/R_* , corresponding to smaller density (Equation (1)). One may expect that the effect of systematics is slowly diminished by accumulating more data taken with different instruments. This is consistent with our experience, that is the initial follow-up light curves without proper treatment of systematics indicated larger impact parameters, and a lower density dwarf star that was inconsistent with the *Hipparcos*-based stellar parameters (Section 3.1). By accumulating more data this inconsistency diminished (Section 3.2). Because both EPD and TFA point toward this direction, and also deliver the smallest formal uncertainty, we expect that the most *accurate* model will be the ELTG in Table 5. This conjecture will be decided with accurate ground-based follow-up photometry (such as presented recently in Johnson et al. 2009), and ultimately when the *Kepler* space mission returns the light curve for HAT-P-11. This will have important implications on optimal trend removal for other transiting systems, where such a space-born “reference” will not be available.

The results for the simultaneous fit using the ELTG systematic model for the follow-up light curves were the following: $T_{c,-231} = 2453217.75466 \pm 0.00187$ (BJD), $T_{c,+91} = 2454605.89132 \pm 0.00032$ (BJD), $K = 11.6 \pm 1.2$ m s^{-1} , $k \equiv e \cos \omega = 0.201 \pm 0.049$, $h \equiv e \sin \omega = 0.051 \pm 0.092$, $R_p/R_* = 0.0576 \pm 0.0009$, $b^2 = 0.120 \pm 0.087$, $\zeta/R_* = 22.15 \pm 0.15$ day^{-1} , and $\gamma = -0.4 \pm 0.8$ m s^{-1} , $B_{\text{instr}} = 0.95 \pm 0.08$, $G_1 = 0.0297 \pm 0.0050$ $\text{m s}^{-1} \text{day}^{-1}$, $M_{0,\text{HATNet}} = 8.35892 \pm 0.00003$ (instrumental HATNet OOT magnitude). The combined and phase-binned light curve of all z -band FLWO 1.2 m observations is shown in Figure 12. The planetary parameters and their uncertainties can be derived by the direct combination of the a posteriori distributions of the light curve, RV, and stellar parameters (see also Pál et al. 2008a). We found that the mass of the planet is $M_p = 0.081 \pm 0.009 M_J$ = $25.8 \pm 2.9 M_\oplus$, the radius is $R_p = 0.422 \pm 0.014 R_J$ = $4.73 \pm 0.16 R_\oplus$, and its density is $\rho_p = 1.33 \pm 0.20$ g cm^{-3} .

Table 6
Orbital and Planetary Parameters

Parameter	Value
Light Curve Parameters	
P (days)	4.8878162 ± 0.0000071
T_c (BJD)	$2454605.89132 \pm 0.00032$
T_{14} (days) ^a	0.0957 ± 0.0012
$T_{12} = T_{34}$ (days) ^a	0.0051 ± 0.0013
a/R_*	$15.58^{+0.17}_{-0.82}$
ζ/R_*	22.15 ± 0.15
R_p/R_*	0.0576 ± 0.0009
$b \equiv a \cos i/R_*$	$0.347^{+0.130}_{-0.139}$
i (deg)	88.5 ± 0.6
Spectroscopic Parameters	
K (m s^{-1})	11.6 ± 1.2
γ (km s^{-1})	-0.4 ± 0.8
G_1 ($\text{m s}^{-1}/\text{day}$)	0.0297 ± 0.0050
k_{RV}^b	0.201 ± 0.049
h_{RV}^b	0.051 ± 0.092
k_C^c	0.190 ± 0.046
h_C^c	-0.016 ± 0.056
e	0.198 ± 0.046
ω	$355^\circ 2 \pm 17^\circ 3$
Secondary Eclipse Parameters^d	
T_s (BJD)	2454608.96 ± 0.15
$T_{s,14}$	0.1006 ± 0.0130
$T_{s,12}$	0.0054 ± 0.0013
Planetary Parameters	
M_p (M_J)	0.081 ± 0.009
R_p (R_J)	0.422 ± 0.014
$C(M_p, R_p)^d$	0.025
ρ_p (g cm^{-3})	1.33 ± 0.20
a (AU)	$0.0530^{+0.0002}_{-0.0008}$
$\log g_p$ (cgs)	3.05 ± 0.06
T_{eq} (K)	878 ± 15
Θ	0.025 ± 0.003
F_{per} ($\text{erg s}^{-1} \text{cm}^{-2}$) ^e	$2.04 \times 10^8 \pm 2.78 \times 10^7$
F_{ap} ($\text{erg s}^{-1} \text{cm}^{-2}$) ^e	$9.11 \times 10^7 \pm 9.53 \times 10^6$
$\langle F \rangle$ ($\text{erg s}^{-1} \text{cm}^{-2}$) ^e	$1.34 \times 10^8 \pm 9.38 \times 10^6$

Notes.

^a T_{14} : total transit duration, time between first to last contact; $T_{12} = T_{34}$: ingress/egress time, time between first and second, or third and fourth contact.

^b Lagrangian orbital elements, based purely on the RV data.

^c Refined values of h and k , derived from RV analysis and the constraint given by the $C_{\text{kh}} \equiv \sqrt{1-e^2}/(1+h)$ value, resulting from the light-curve modeling and stellar evolution analysis.

^d Correlation coefficient between the planetary mass M_p and radius R_p .

^e Occultation parameters and incoming flux per unit surface area in periastron, apastron, and average for the orbit were calculated using the refined values k_C and h_C .

The final planetary parameters are summarized at the bottom of Table 6.

5.5. Constraints on Orbital Eccentricity

An interesting aspect of the HAT-P-11 system is that the light-curve analysis, the *Hipparcos* parallax, and the theoretical isochrones together provide an extra constraint on the orbital eccentricity. In our analysis, the orbital eccentricity and argument of pericenter are characterized by the Lagrangian orbital elements $k = e \cos \omega = 0.201 \pm 0.049$ and $h = e \sin \omega = 0.051 \pm 0.092$. If the analysis relied purely on the RV data, then the errors in k and h would be similar, the error of h being somewhat smaller (see Section 2.4). However, when the data are

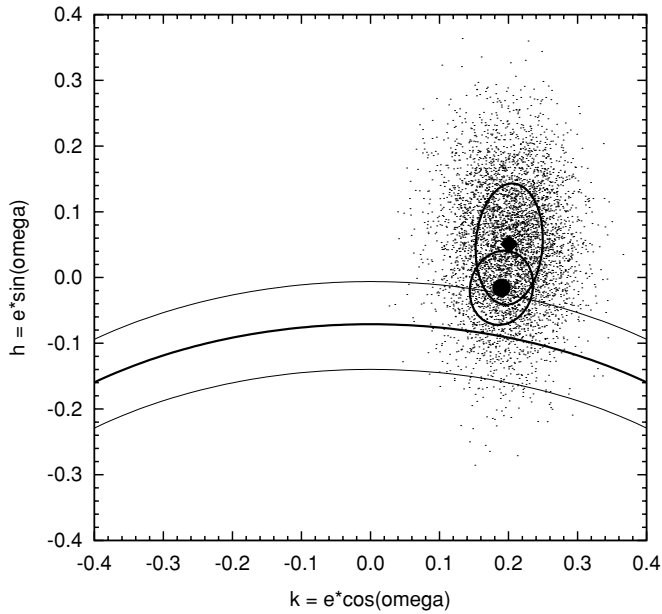


Figure 13. Cloud of points represent the a posteriori distribution of the orbital elements $k = e \cos \omega$ and $h = e \sin \omega$ yielded by the global modeling (Section 5.4). The best-fit (k, h) pair is marked as a filled diamond, encircled with the 1σ confidence ellipsoid. The constraint given by the $C_{kh} \equiv \sqrt{1 - e^2}/(1+h)$ quantity defines a stripe in the (h, k) plane. The location of the finally accepted (k, h) value and its 1σ confidence are denoted by the dot below the diamond and the surrounding ellipse, respectively.

complemented with photometry of transit events (as in our case), the period and phase of the orbit become tightly constrained. As a result, the k and h orbital elements will have different uncertainties, since the mean longitude at the transit is constrained more by $\cos \omega$ than $\sin \omega$ (this is due to the same underlying reason that the phase lag between the secondary and primary transits is also proportional to $e \cos \omega$ and does not strongly depend on $e \sin \omega$). Indeed, the a posteriori distribution of h and k as yielded by the joint analysis (Section 5.4) is asymmetric, and the uncertainty in k is half of the uncertainty in h (Figure 13, large oval around the filled diamond).

By re-arranging Equation (2), we can define C_{kh} as

$$C_{kh} \equiv \frac{\sqrt{1 - h^2 - k^2}}{1 + h} = \frac{a}{R_\star} \left(\frac{\zeta}{R_\star} \right)^{-1} \frac{n}{\sqrt{1 - b^2}}, \quad (3)$$

where $n = 2\pi/P$ is the mean motion (see also Ford et al. 2008). The period P , impact parameter b , and ζ/R_\star are well constrained by the photometry of multiple transit events. The normalized semimajor axis a/R_\star is determined from the apparent magnitudes, *Hipparcos* parallax and isochrones, as described in Section 3.2. These together yield an estimate of $C_{kh} = 0.931 \pm 0.063$, independent of the RV data, and thus provide an additional constraint on h and k in the form of a hyperbola on the $k - h$ plane. Taking into account the uncertainties in C_{kh} , this appears as a stripe in the $k - h$ plane (Figure 13). This constraint can be used to decrease the uncertainty of h by a factor of 2, so that it becomes similar to that of k .

In practice, we have a Monte Carlo distribution for k , h , and C_{kh} . For each k and h value in MC distribution, we determine the closest k' , h' point of the hyperbola (there is a unique solution for this). Since the value for C_{kh} constrains only one degree of freedom, we can treat (k, h) and (k', h') as independent. Therefore, we define k_C and h_C as the mean of k , k' and h , h' , respectively, and consider these as an improved estimate of the

orbital eccentricity parameters. The result is an MC distribution for k_C and h_C , where their mean values and errors can be derived: $k_C = 0.190 \pm 0.046$ and $h_C = -0.016 \pm 0.056$. Indeed, the errors in k_C and h_C are now comparable.

Based on k_C and h_C , the refined orbital eccentricity is $e = 0.198 \pm 0.046$, and the argument of pericenter is $\omega = 355.2 \pm 17.3$. Note that the above method is unique, and can be applied for eccentric transiting systems with well known parallax but poorly determined RV orbit. It is likely that the *Kepler* mission will find similar cases. A counter example is HAT-P-2b (Bakos et al. 2007), where the RV amplitude is large compared to the uncertainties (1 km s^{-1}), and the error in the parallax is larger, thus h cannot be refined. The current analysis points toward an even more general way of simultaneously fitting to *all* data, including the stellar isochrone search with various constraints (e.g., parallax information with error bars).

6. DISCUSSION

6.1. The Planet HAT-P-11b

The stellar parameter determination (Section 3), the blend analysis (Section 4), and the global modeling of the data presented in Section 5 together show the detection of a $25.8 \pm 2.9 M_\oplus$ and $4.73 \pm 0.16 R_\oplus$ planet that orbits a bright ($V = 9.59$) K4 dwarf star on an eccentric ($e = 0.198 \pm 0.046$) orbit with $P = 4.8878$ day period, causing a $11.6 \pm 1.2 \text{ m s}^{-1}$ RV variation of the host star and a 4.2 mmag transit as it passes in front of the star. The planet is somewhat more massive than our own Uranus ($14.3 M_\oplus$) and Neptune ($17.1 M_\oplus$), and slightly more massive than GJ 436b ($22.6 M_\oplus$). Based on its mass and radius, it is justified to use the metonym super-Neptune for classification of HAT-P-11b, just like for GJ 436b, the only similar object known so far. For the location of \sim Neptune-mass objects, see Figure 14.

When compared to models of Fortney et al. (2007), HAT-P-11b is much smaller in radius than similar mass planets with 50% rock/ice core and 50% H/He envelope, and HAT-P-11b is much bigger than pure rock/ice planets without a gas envelope. The mismatch with such pure-rock/ice “super-Earths” is confirmed by models of Valencia et al. (2007). Overlaid in Figure 14 are super-Earth planet models with Earth-like composition (lower dotted line) and 50% by mass H_2O content and Earth-like Si/Fe ratio (upper dotted line). Both models fall clearly below the observational values for HAT-P-11b. As the expected limit for gravitational capture of H/He is $\sim 10 M_\oplus$ (Rafikov 2006), it is hardly surprising that HAT-P-11b has some H/He, even if evaporation played an important role during its evolution. HAT-P-11b receives only modest irradiation when compared to hot Jupiters. The time-averaged flux over its eccentric orbit is $1.34 \times 10^8 \pm 9.38 \times 10^6 \text{ erg s}^{-1} \text{ cm}^{-2}$, and the equivalent semimajor axis where similar irradiation would be received from a Sun-like star is $a_{\text{equiv}} \sim 0.1 \text{ AU}$. Using the models from Fortney et al. (2007), the radius of HAT-P-11b is indeed consistent with a 90% heavy element planet with an irradiation corresponding to $a_{\text{equiv}} = 0.1 \text{ AU}$. In these models, the heavy elements are located in the core, and the envelope is metal-free.

We also compared the observational values to the thorough theoretical work of Baraffe et al. (2008). Planetary isochrones for various metal content, age, and irradiation are also plotted in Figure 14. As Fortney et al. (2007) note, planetary radii and their evolution are scarcely affected when irradiation is small, and $a_{\text{equiv}} \gtrsim 0.1 \text{ AU}$; thus, it is expected that HAT-P-11b will

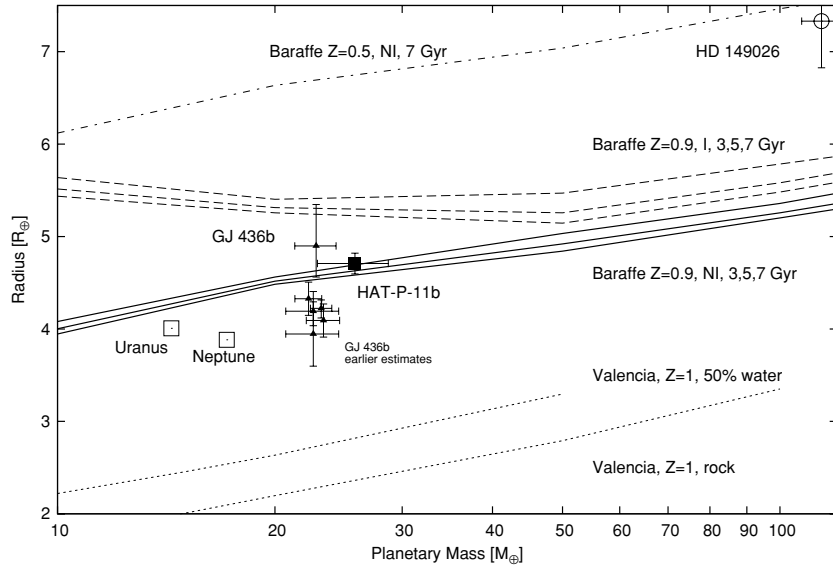


Figure 14. Mass–radius diagram for Neptune-mass planets. Plotted are Uranus and Neptune from our own Solar system, the detection presented in this paper, HAT-P-11b, and the only other known transiting hot Neptune GJ 436b. For GJ 436b, we plotted all available mass and radius determinations (Southworth 2009), the most recent one being the highest point in radius. Also shown in the upper right corner is the hot Saturn HD 149026b. Overplotted in the figure are theoretical models. HAT-P-11b is clearly much bigger than a $\sim 25.8 \pm 2.9 M_{\oplus}$ rocky or water-rich “super-earth” would be, as based on models from Valencia et al. (2007). HAT-P-11b is also inconsistent with irradiated extreme metal-rich ($Z = 0.9$) models of Baraffe et al. (2008) (labeled as “Baraffe Z = 0.9, I, 3,5,7 Gyr,” “I” stands for irradiated). Indeed, these models assume $a_{\text{equiv}} = 0.045$ AU semimajor axis around a solar twin, instead of the low irradiation received by HAT-P-11b ($a_{\text{equiv}} = 0.1$ AU). The $Z = 0.5$ models from Baraffe et al. (2008) with a 50% H/He envelope lie on the top of the figure, clearly presenting a mismatch with HAT-P-11b. However, HAT-P-11b is fully consistent with $Z = 0.9$ metal-rich non-irradiated (“NI”) Baraffe et al. (2008) models (thick lines), in particular with the 3–5 Gyr models.

match non-irradiated models better, and indeed, the best match is with extreme metal rich non-irradiated Baraffe models with $Z = 0.9$ fraction of heavy elements (rock and ice), and a 10% H/He envelope. The non-irradiated metal-rich models of various ages between 3 and 7 Gyr lie very close to each other and are all within the observational error bars. However, the non-irradiated models with significant (50%) H/He envelope (top of figure) are far from matching the observations. Baraffe et al. (2008) note that, in general, the distribution of the heavy elements (core versus envelope) can have considerable impact on the planetary radius, but in this extreme metal-rich scenario, the freedom to vary their distribution is limited. Altogether, HAT-P-11b appears to be a super-Neptune planet with $Z = 0.9$ and with a 10% H/He envelope.

It is interesting to compare HAT-P-11b to GJ 436b—the only other super-Neptune with known mass and radius. These two planets are very similar in some physical properties in spite of the very different environment. There are numerous system parameter determinations for GJ 436b available in the literature (see compilation and Table A11 of Southworth 2009). Starting from the discovery of the transits by Gillon et al. (2007a) ($22.6 M_{\oplus}$, $3.95 R_{\oplus}$), planetary masses range from $M_p = 22.26 M_{\oplus}$ to $24.8 M_{\oplus}$, and planetary radii range from $3.95 R_{\oplus}$ to $4.9 R_{\oplus}$ (Bean et al. 2008). Some of these earlier estimates, including that of Bean et al. (2008), are plotted in Figure 14. The RV amplitude of GJ 436 ($K = 18.34 \pm 0.52 \text{ m s}^{-1}$; T08) is larger and better determined than HAT-P-11b ($K = 11.6 \pm 1.2 \text{ m s}^{-1}$), and the transits are deeper (6.5 mmag versus 4.2 mmag), and have even been observed from space by *Spitzer* (Gillon et al. 2007b; Deming et al. 2007) and *Hubble Space Telescope* (Bean et al. 2008). The reasons for the larger K value and transit depth of GJ 436, however, are due to the host star being a small mass and radius M dwarf ($M_{\star} \approx 0.45 M_{\odot}$, $R_{\star} \approx 0.46 R_{\odot}$, T08 and Southworth 2009). Uncertainties in both the planetary mass and radius remain con-

siderable because of the uncertainty in the stellar parameter determination for M dwarf stars (T08). Altogether, the masses and radii of GJ 436b and HAT-P-11b are very close (to within 2σ). GJ 436b has a slightly smaller and better determined mass. HAT-P-11b has a comparable and somewhat better determined radius.

There are other similarities between the two planets. Both orbit on short period mildly eccentric orbits, GJ 436b: $e = 0.16 \pm 0.02$ (Gillon et al. 2007a) and HAT-P-11b: $e = 0.198 \pm 0.046$. The fact that they have not circularized yet is interesting, as the circularization timescale appears shorter than the age of the host stars (e.g., Matsumura et al. 2008, and references therein), although the stellar ages are ill determined due to the unevolved M and K dwarf host stars. As Matsumura et al. (2008) noted on the origins of eccentric close-in planets, some of these planets may have larger than expected Q specific dissipation functions (depending on the planetary structure, and characteristics of the tides). The fact that neither of these hot Neptunes has circularized yet may tell us something about the formation and planetary structure of Neptunes. We note that the putative HAT-P-11c planet (Section 6.2) causing the long-term drift in the data appears to have a large semimajor axis, because the RV drift does not show any significant nonlinear coefficient over the one year timescale of the observations (Section 2.4). Thus, it is unlikely that it is causing eccentricity pumping. Whether the Kozai mechanism (Fabrycky & Tremaine 2007) plays an important role will be subject to further investigations when the long-term drift in the RVs is better characterized. Both GJ 436b and HAT-P-11b have similar surface gravities, $\log g_p = 3.11 \pm 0.04$ (cgs, T08) for GJ 436b versus $\log g_p = 3.05 \pm 0.06$ for HAT-P-11b. They also appear to have similar mean densities, $\rho_p = 1.69 \pm 0.14 \text{ g cm}^{-3}$ (T08) for GJ 436b and $1.33 \pm 0.20 \text{ g cm}^{-3}$ for HAT-P-11b.

It is surprising that in spite of these similarities (mass, radius, density, surface gravity, eccentricity), the two planets are

in grossly different environments. Consequently, the GJ 436b–HAT-P-11b pair must yield tight constraints on theories that should reproduce their properties in spite of the different environments. GJ 436b orbits an M dwarf with half the mass and radius of HAT-P-11, one-tenth of the luminosity ($L_{\star} = 0.026 L_{\odot}$ versus $0.26 \pm 0.02 L_{\odot}$), and colder effective temperature of $T_{\text{eff}\star} = 3350 \pm 300$ K (T08) versus 4780 ± 50 K for HAT-P-11b. The smaller semimajor axis of GJ 436b compensates to some extent for the lower luminosity host star, but still, the irradiation they receive is grossly different (GJ 436b: $3.2 \times 10^7 \text{ erg s}^{-1} \text{ cm}^{-2}$, HAT-P-11b: $1.34 \times 10^8 \text{ erg s}^{-1} \text{ cm}^{-2}$, i.e., 4 times more, as time integrated over the eccentric orbit). These lead to different expected equilibrium temperatures: 650 ± 60 K for GJ 436b (T08) versus 878 ± 15 K, assuming complete heat redistribution. Also, the different stellar effective temperatures lead to different spectral distributions of the infalling flux. It will be interesting to compare the atmospheric properties of the two planets to see the effect of different integrated flux and spectral flux distributions on these otherwise similar planets.

While both GJ 436b and HAT-P-11b have similar mass and radius, and inferred structure of $Z = 0.9$ heavy element content with 10% H/He envelope, it is worth noting that the metallicity of the host stars, and presumably the environment these planets formed in, is different; $[\text{Fe}/\text{H}] = -0.03 \pm 0.20$ for GJ 436 (T08) and $[\text{Fe}/\text{H}] = +0.31 \pm 0.05$ for HAT-P-11.

From the observational point of view, HAT-P-11 is a bright star ($V \sim 9.58$), more than a magnitude brighter than GJ 436. The transits of HAT-P-11b are at a small impact parameter ($b = 0.347^{+0.130}_{-0.139}$) as compared to the near-grazing transit of GJ 436b ($b = 0.848$). The total duration of the transit for HAT-P-11b is about twice (0.0957 ± 0.0012 days) that of GJ 436b (0.042 days). We can thus expect very high-quality follow-up observations of HAT-P-11b in the future.

6.2. A Second Planet in the System?

The RV of HAT-P-11 shows, in addition to the 4.8878 day period induced by HAT-P-11b, a significant trend of $G_1 = 0.0297 \pm 0.0050 \text{ m s}^{-1} \text{ day}^{-1}$. This drift could be due to a second planet in the system, corresponding to $M_2 \sin i_2 / a_2^2 \sim \dot{G}_1 / G = (0.061 \pm 0.01) M_J \text{ AU}^{-2}$, where the subscript “2” refers to HAT-P-11c, and G is the gravitational constant. Such a conjecture is scarcely surprising: for example, Bouchy et al. (2009) have noted that 16 out of the 20 hot Neptune planets discovered heretofore are members of multiple planet systems. Interestingly enough, as pointed out by Bouchy et al. (2009), this fraction (80%) is significantly higher than 23%, which is the fraction of all known exoplanets which are in multiple systems. We also recall that the significant orbital eccentricity of HAT-P-11b is reminiscent of that of GJ 436b, and that the latter has motivated the speculation that there may be another planet in the system, sufficient to maintain the eccentricity of GJ436b (Ribas et al. 2008; Bean & Seifahrt 2008). Finally, as was also pointed out by Bouchy et al. (2009), of seven multiple planet systems containing both a gas-giant planet and a hot Neptune planet, all have super-solar metallicities. The high metallicity of HAT-P-11, $[\text{Fe}/\text{H}] = +0.31 \pm 0.05$, then strengthens the suspicion that there may be multiple planets in the system.

Continued monitoring of the RV of HAT-P-11 over the next few years should indicate whether the drift persists and whether it shows evidence of curvature of the orbit. Another way to establish the presence of a second body in the system is to

search for TTVs in repeated transits (Agol et al. 2005; Holman & Murray 2005).

6.3. Future Kepler Observations

The fact that HAT-P-11 will lie on one of the detector chips for the *Kepler* spacecraft presents remarkable opportunities for scientific follow-up of the discovery presented here. If all goes well, *Kepler* should be capable of 1 minute cadence photometry at a precision of 0.1 mmag for this bright star. Currently, *Kepler* is expected to be operational for a minimum of 3.5 years, and perhaps longer; in that time it should have more than 250 transits by HAT-P-11b. In addition, it should show photometric variability due to surface inhomogeneities such as starspots, spanning more than 40 rotations if indeed the rotation period of the planet is verified to be about 29.2 days. Here we list some opportunities for important scientific follow-up with *Kepler*:

Kepler transit data. With a depth of 4.2 mmag, the transit light curve of HAT-P-11b should be measurable by *Kepler* with excellent precision for a single light curve and extraordinary precision when many light curves are combined. To maximize the accuracy of parameters derived for the HAT-P-11 system, it is important that, in addition to the *Kepler* observations, precise ground-based RV data be obtained through the duration of the *Kepler* observations.

The possibility of a second planet in the system can be tested through a search for TTVs in the large number of transits to be observed by *Kepler*. As noted above, RV data obtained over the same time frame could provide independent evidence for such a planet, and comparison of the two data sets would be of obvious importance.

Kepler OOT photometry. The *Kepler* data should reveal the detailed modulation of photospheric brightness—presumably due to starspot activity—with great precision and time coverage over the lifetime of the mission. This could yield much useful information about the star, including its rotation and even differential rotation (Fröhlich 2007). Furthermore, if multiple transits of HAT-P-11b pass in front of the same starspot on the face of the slowly rotating star, then extraordinary precision can be achieved in determining the rotation rate (Silva-Valio 2008). Comparison with concurrent ground-based measurements of the chromospheric emission S index will enable investigation of how photospheric spots correlate with chromospheric emission on stars other than the sun. As noted earlier, the data on S index reported here show a long-term (~ 450 day) variation reminiscent of solar activity cycles; monitoring both photospheric emission variations from *Kepler* broadband photometry and chromospheric emission variations from ground based telescopes could prove to be useful.

Kepler asteroseismology. *Kepler* will obtain extraordinary information about the internal structure and evolution of stars from asteroseismic investigations, which measure the frequencies and amplitudes of acoustic oscillation modes (“ p -modes”) through small changes in the integrated brightness of the star. The “large splitting” of p -mode frequencies yields direct information on the radius of the star, and their “small splitting” gives information on the H/He ratio in the core and hence the age of the star (e.g., Christensen-Dalsgaard 2004). A great deal of additional information is possible if the star is accompanied by a transiting planet (like HAT-P-11b); in this case, the transit light curves yield completely independent information on the radius and mean density of the star. An additional bonus in the case of HAT-P-11 is that it has an excellent *Hipparcos* parallax. Combining these independent pieces of information should lead

to very detailed knowledge of its internal structure, including second-order near-surface effects not accounted for in normal interior structure models (Kjeldsen et al. 2008). Information on the age of the star, if it can be obtained from measurement of the small splitting, could provide a useful comparison with the age inferred either from the global (light curve, RV, stellar isochrone) modeling of the data or from the Ca HK index.

As noted above, there is a suggestion from the variation of its S index that HAT-P-11 is undergoing long-term variations of its surface magnetic activity somewhat reminiscent of the solar activity cycle. On the Sun, solar cycle-related variations of solar magnetic activity are known to be correlated with frequency variations of p -modes (e.g., Woodard & Noyes 1985; Woodard et al. 1991), because the sub-surface structure is modified in regions of solar magnetic activity. Monitoring the p -mode frequencies of HAT-P-11 over the course of the *Kepler* mission, along with continued ground-based monitoring of the S -index, may show whether similar behavior occurs in the sub-surface layers of another star with significantly different structure.

Finally, we note that two other stars with known transiting planets, namely, TrES-2 (O’Donovan et al. 2006) and HAT-P-7 (Pál et al. 2008a), also lie on the *Kepler* detector array, so it should be possible to carry out studies of these stars and their planets similar to those described above for the HAT-P-11 system. It would be interesting to compare the results for these two stars, with spectral type F and G, respectively, with those for the K star HAT-P-11. Almost certainly many more TEP systems will be discovered by *Kepler*, but those systems that are known in advance of the mission should be especially valuable since observations with the 1 minute cadence can be scheduled from the start of the mission, plus the longer baseline improves our sensitivity to detect secular changes.

HATNet operations have been funded by NASA grants NEG04GN74G, NNX08AF23G, and SAO IR&D grants. Work by G.Á.B. and J.A.J. was supported by Postdoctoral Fellowships of the NSF Astronomy and Astrophysics Program (AST-0702843 and AST-0702821, respectively). We also acknowledge partial support from the *Kepler* Mission under NASA Cooperative Agreement NCC2-1390 (PI: D.W.L.). G.K. thanks the Hungarian Scientific Research Foundation (OTKA) for support through grant K-60750. This research has made use of Keck telescope time granted through NOAO (program A285Hr) and NASA (N128Hr). Data presented herein were obtained at the W. M. Keck Observatory from telescope time allocated to NASA through the agency’s scientific partnership with the California Institute of Technology and the University of California. The Observatory was made possible by the generous financial support of the W. M. Keck Foundation.

APPENDIX

SYSTEMATIC VARIATIONS

As regards the red-noise or systematic variations (also referred to as “trends”), we may distinguish between those effects that have a well understood reason, and where deviations correlate with a set of external parameters, and other systematic variations where the underlying parameters are not known. The deviations are usually taken with respect to the median of the light curve.

The $m(t_i)$ light curve of a star observed at t_i time instances can be decomposed as

$$m(t_i) = m_0(\vec{p}, t_i) + G(t_i) + E(\vec{e}_i(t_i)) + T(t_i), \quad (\text{A1})$$

where $m_0(\vec{p}, t_i)$ is the systematics-free light curve as a function of time, and parameterized by a discrete set of parameters denoted as \vec{p} , $G(t_i)$ is white noise, E is the systematic variation due to the change in external parameters \vec{e}_i , and T denotes the additional trend that is *not* known to be simple function of such parameters. For planetary transits, the functional form of m_0 can be a transit model by Mandel & Agol (2002), and the \vec{p} parameters can be the a/R_* geometric semimajor axis, $p \equiv R_*/R_p$ relative diameter of the planet, the normalized impact parameter b and the T_c center of transit. For a δ Scuti variable star, these parameters can be the amplitudes and phases of various Fourier components.

A.1. External Parameter Decorrelation

Although briefly described earlier (Bakos et al. 2007), it is worth defining the EPD technique, since it is extensively used in this work. The EPD method attempts to determine the actual functional form of E in Equation (A1). The EPD effects are treated and determined as specific for each star, i.e., no information from other stars are used (this is a key difference when compared to TFA that uses a template of other stars—see below).

Constant (or simple) EPD. The simplest form of EPD is when we assume that the underlying m_0 signal is constant, and also that $\langle E \rangle \gtrsim \langle T \rangle$ (i.e., the effects to be corrected by EPD are of the same order as those corrected by TFA). A typical application is for planetary transits in survey mode, since such transits are short events compared to the total orbital time, and have mostly been observed around stars with much smaller variation than the transit amplitude (note that there are exceptions; see Alonso et al. 2008); thus the underlying signal can be approximated with its median $\sim 95\%$ of the time. The E relation between $\delta m(t_i) \equiv m(t_i) - m_0(t_i) = m(t_i) - \langle m(t_i) \rangle_m$ and $e_i(t_i)$ parameters is sought via a χ^2 minimization, usually by nonlinear least-squares method with outlier rejection ($\langle \rangle_m$ denotes the median value). Upon determining E , we get an EPD corrected signal $\delta m_{\text{EPD}}(t_i) = \delta m(t_i) - E(t_i)$.

Our experience with HATNet survey data has shown that the effects of E and T are indeed comparable, and thus we use constant EPD. Specifically, the external parameters are the X,Y sub-pixel position, the background and its standard deviation, the stellar profile parameters characterizing the point-spread function width (called S) and its elongation (D and K), plus the hour angle and zenith distance.

Simultaneous EPD. Used primarily in the analysis of the photometric follow-up data, where most of the observations are centered on the transits; thus, the assumption of constant signal does not hold. One possibility is to use the OOT section of the light curve to determine the EPD parameters in a constant EPD mode, and then apply the correction for the in-transit section of the light curve as well. This is sub-optimal, as the OOT may be very short compared to the in-transit section, or may be missing. Thus, the key difference compared to constant EPD is that we use all data to recover the dependence on external parameters, i.e., $m_0(\vec{p}, t_i)$ in Equation (A1) is not constant, but assumed to be a function of other parameters and time. The fitting procedure determines both the E correlation and the optimal set of \vec{p} parameters simultaneously.

A.2. The Trend Filtering Algorithm

The signal after (or without) the EPD procedure still contains the general systematic variations denoted as $T(t_i)$ in

Equation (A1). These are suppressed by the Trend Filtering Algorithm (TFA; see Kovács et al. 2005), assuming that certain other stars in an M element light-curve “template” show similar variations.

To recall, for selected star j , TFA minimizes the following expression:

$$D = \sum_{i=1}^N \left[m_j(t_i) - m_{j,0}(\vec{p}, t_i) - F_M(t_i) - E_j(\vec{e}(t_i)) \right]^2, \quad (\text{A2})$$

where

$$F_M(t_i) = \sum_{k=1, k \neq j}^{k=M} c_k m_k(t_i) \quad (\text{A3})$$

is the TFA filter function of M elements. The notation is like above in Equation (A1), $m_{j,0}(\vec{p}, t_i)$ is the model function, and E_j is the EPD correction.

There are many variants of TFA, and they have been used widely in this work. The signal search in the HATNet data is done in two parallel steps. First via *simple (or constant) TFA* where there is no assumption on the periodicity, the model function $m_{j,0}$ is a constant, E_j is zero, as EPD has been performed as an independent step before TFA, and the c_k coefficients are sought. Second, via *reconstructive TFA*, where the simple TFA is followed by a frequency search, the signal is phase-folded with the most significant frequency, the model function $m_{j,0}$ is fitted to the folded data, the model function is unwrapped to the original time base, and D is minimized again to iteratively determine the c_k coefficients. The third method, introduced in this work, is *simultaneous TFA*, whereby the c_k TFA coefficients and the functional dependence of $m_j(\vec{p}, t_i)$ on \vec{p} parameters are simultaneously determined.

EPD and TFA can be performed sequentially, or even simultaneously. In the analysis of the photometric follow-up data (see Section 2.3), we implemented such a *simultaneous EPD–TFA*, where the $E_j(\vec{e})$ EPD function is simultaneously fitted with the c_k TFA template coefficients and the m_j model function.

Both TFA and EPD can be performed *globally*, using one set of coefficients for the entire data set, and *locally*, when Equation (A2) is split up into smaller data blocks, such as one-night segments, and the c_k TFA coefficients and the EPD function parameters are fitted for each data block separately to allow for changing systematics. Conversely, for *global TFA* systematic variations of template stars have to “match” those of the main target (minus the model) for all nights.

Finally, we note that if we do not use EPD (eliminate the term for E in Equation (A1)), but apply TFA only, then naturally, TFA will take care of some of the systematics that otherwise would have been corrected by EPD.

REFERENCES

- Agol, E., Steffen, J., Sari, R., & Clarkson, W. 2005, *MNRAS*, **359**, 567
- Alonso, R., et al. 2008, *A&A*, **482**, L21
- Bakos, G. Á., Lázár, J., Papp, I., Sári, P., & Green, E. M. 2002, *PASP*, **114**, 974
- Bakos, G. Á., Noyes, R. W., Kovács, G., Stanek, K. Z., Sasselov, D. D., & Domsa, I. 2004, *PASP*, **116**, 266
- Bakos, G. Á., et al. 2007, *ApJ*, **670**, 826
- Bakos, G. Á., et al. 2009, *ApJ*, **696**, 1950
- Baraffe, I., Chabrier, G., Allard, F., & Hauschildt, P. H. 1997, *A&A*, **327**, 1054
- Baraffe, I., Chabrier, G., Allard, F., & Hauschildt, P. H. 1998, *A&A*, **337**, 403
- Baraffe, I., Chabrier, G., & Barman, T. 2008, *A&A*, **482**, 315
- Bean, J. L., & Seifahrt, A. 2008, *A&A*, **487**, L25
- Bean, J. L., et al. 2008, *A&A*, **486**, 1039
- Barbieri, M., et al. 2007, *A&A*, **476**, L13
- Bouchy, F., et al. 2005, *A&A*, **444**, L15
- Bouchy, F., et al. 2009, *A&A*, **496**, 527
- Brown, T. M., Charbonneau, D., Gilliland, R. L., Noyes, R. W., & Burrows, A. 2001, *ApJ*, **552**, 699
- Burrows, A., Hubeny, I., Budaj, J., & Hubbard, W. B. 2007, *ApJ*, **661**, 502
- Butler, R. P., Vogt, S. S., Marcy, G. W., Fischer, D. A., Wright, J. T., Henry, G. W., Laughlin, G., & Lissauer, J. J. 2004, *ApJ*, **617**, 580
- Butler, R. P., et al. 1996, *PASP*, **108**, 500
- Carpenter, J. M. 2001, *AJ*, **121**, 2851
- Carter, J. A., Yee, J. C., Eastman, J., Gaudi, B. S., & Winn, J. N. 2008, *ApJ*, **689**, 499
- Casagrande, L., Portinari, L., & Flynn, C. 2006, *MNRAS*, **373**, 13
- Charbonneau, D., Brown, T. M., Latham, D. W., & Mayor, M. 2000, *ApJ*, **529**, L45
- Charbonneau, D., Brown, T. M., Noyes, R. W., & Gilliland, R. L. 2002, *ApJ*, **568**, 377
- Charbonneau, D., et al. 2005, *ApJ*, **626**, 523
- Christensen-Dalsgaard, J. 2004, *Sol. Phys.*, **220**, 137
- Claret, A. 2004, *A&A*, **428**, 1001
- Demarque, P., Woo, J.-H., Kim, Y.-C., & Yi, S. K. 2004, *ApJS*, **155**, 667
- Deming, D., Harrington, J., Laughlin, G., Seager, S., Navarro, S. B., Bowman, W. C., & Horning, K. 2007, *ApJ*, **667**, L199
- Droege, T. F., Richmond, M. W., & Sallman, M. 2006, *PASP*, **118**, 1666
- Fabrycky, D., & Tremaine, S. 2007, *ApJ*, **669**, 1298
- Fischer, D. A., et al. 2007, *ApJ*, **669**, 1336
- Ford, E. 2006, *ApJ*, **642**, 505
- Ford, E. B., Quinn, S. N., & Veras, D. 2008, *ApJ*, **678**, 1407
- Fortney, J. J., Marley, M. S., & Barnes, J. W. 2007, *ApJ*, **659**, 1661
- Fröhlich, H.-E. 2007, *Astron. Nachr.*, **328**, 1037
- Gillon, M., et al. 2007a, *A&A*, **472**, L13
- Gillon, M., et al. 2007b, *A&A*, **471**, L51
- Girardi, L., Bressan, A., Bertelli, G., & Chiosi, C. 2000, *A&AS*, **141**, 371
- Gray, D. F. 1988, *Lectures on Spectral-line Analysis: F, G, and K Stars* (Avra: The Publisher)
- Gray, D. F. 1992, *The Observation and Analysis of Stellar Photospheres* (Camb. Astrophys. Ser., Vol. 20; Cambridge: Cambridge Univ. Press)
- Henry, G. W., Marcy, G. W., Butler, R. P., & Vogt, S. S. 2000, *ApJ*, **529**, L41
- Holman, M. J., & Murray, N. W. 2005, *Science*, **307**, 1288
- Johnson, J. A., Winn, J. N., Cabrera, N. E., & Carter, J. A. 2009, *ApJ*, **692**, L100
- Johnson, J. A., et al. 2008, *ApJ*, **686**, 649
- Kjeldsen, H., Bedding, T. R., & Christensen-Dalsgaard, J. 2008, *ApJ*, **683**, L175
- Kovács, G., Bakos, G. Á., & Noyes, R. W. 2005, *MNRAS*, **356**, 557
- Kovács, G., Zucker, S., & Mazeh, T. 2002, *A&A*, **391**, 369
- Latham, D. W. 1992, in *ASP Conf. Ser. 32, Complementary Approaches to Double and Multiple Star Research*, ed. H. A. McAlister & W. I. Hartkopf (San Francisco, CA: ASP), **110**
- Latham, D. W., et al. 2009, *ApJ*, **704**, 1107
- Leger, A., et al. 2009, *A&A*, **506**, 287
- Lovis, C., et al. 2006, *Nature*, **441**, 305
- Matsumura, S., Takeda, G., & Rasio, F. A. 2008, *ApJ*, **686**, L29
- Mandel, K., & Agol, E. 2002, *ApJ*, **580**, L171
- Marcy, G. W., & Butler, R. P. 1992, *PASP*, **104**, 270
- Mayor, M., et al. 2003, *The Messenger*, **114**, 20
- Mayor, M., et al. 2009, *A&A*, **493**, 639
- McArthur, B. E., et al. 2004, *ApJ*, **614**, L81
- McLaughlin, D. B. 1924, *ApJ*, **60**, 22
- Monet, D. 1998, *USNO-A2.0 Catalogue*, US Naval Observatory
- Noyes, R. W., Hartmann, L. W., Baliunas, S. L., Duncan, D. K., & Vaughan, A. H. 1984, *ApJ*, **279**, 763
- O’Donovan, F. T., et al. 2006, *ApJ*, **651**, L61
- Pál, A., & Bakos, G. Á. 2006, *PASP*, **118**, 1474
- Pál, A., et al. 2008a, *ApJ*, **680**, 1450
- Pál, A. 2008b, *MNRAS*, **390**, 281
- Perryman, M. A. C., et al. 1997, *A&A*, **323**, 49
- Pont, F., Zucker, S., & Queloz, D. 2006, *MNRAS*, **373**, 231
- Press, W. H., Teukolsky, S. A., Vetterling, W. T., & Flannery, B. P. 1992, in *Numerical Recipes in C: The Art of Scientific Computing*, (2nd ed.; Cambridge: Cambridge Univ. Press)
- Protopapas, P., Jimenez, R., & Alcock, C. 2005, *MNRAS*, **362**, 460
- Queloz, D., et al. 2001, *A&A*, **379**, 279
- Rafikov, R. R. 2006, *ApJ*, **648**, 666
- Ramírez, I., & Meléndez, J. 2005, *ApJ*, **626**, 465
- Ribas, I., Font-Ribera, A., & Beaulieu, J.-P. 2008, *ApJ*, **677**, L59
- Rivera, E. J., et al. 2005, *ApJ*, **634**, 625
- Rossiter, R. A. 1924, *ApJ*, **60**, 15
- Santos, N. C., et al. 2004, *A&A*, **426**, L19
- Sato, B., et al. 2005, *ApJ*, **633**, 465

- Seager, S., Kuchner, M., Hier-Majumder, C. A., & Militzer, B. 2007, *ApJ*, **669**, 1279
- Seagroves, S., Harker, J., Laughlin, G., Lacy, J., & Castellano, T. 2003, *PASP*, **115**, 1355
- Silva-Valio, A. 2008, *ApJ*, **683**, L179
- Skrutskie, M. F., et al. 2006, *AJ*, **131**, 1163
- Skumanich, A. 1972, *ApJ*, **171**, 565
- Soderblom, D. R., Duncan, D. K., & Johnson, D. R. H. 1991, *ApJ*, **375**, 722
- Southworth, J. 2009, *MNRAS*, **394**, 272
- Sozzetti, A., et al. 2007, *ApJ*, **664**, 1190
- Tingley, B., & Sackett, P. D. 2005, *ApJ*, **627**, 1011
- Torres, G., Konacki, M., Sasselov, D. D., & Jha, S. 2005, *ApJ*, **619**, 558
- Torres, G., Winn, J. N., & Holman, M. J. 2008, *ApJ*, **677**, 1324
- Torres, G., et al. 2007, *ApJ*, **666**, 121
- Udry, S., et al. 2007, *A&A*, **469**, L43
- Valenti, J. A., & Fischer, D. A. 2005, *ApJS*, **159**, 141
- Valenti, J. A., & Piskunov, N. 1996, *A&AS*, **118**, 595
- Vogt, S. S., et al. 1994, *Proc. SPIE*, **2198**, 362
- Valencia, D., Sasselov, D. D., & O'Connell, R. J. 2007, *ApJ*, **665**, 1413
- West, R. G., et al. 2009, *A&A*, **502**, 395
- Winn, J. N., Henry, G. W., Torres, G., & Holman, M. J. 2008, *ApJ*, **675**, 1531
- Winn, J. N., et al. 2005, *ApJ*, **631**, 1215
- Woodard, M. F., Libbrecht, K. G., Kuhn, J. R., & Murray, N. 1991, *ApJ*, **373**, L81
- Woodard, M. F., & Noyes, R. W. 1985, *Nature*, **318**, 449
- Yi, S. K., et al. 2001, *ApJS*, **136**, 417